Radio Spectral Energy Distribution of Low-z Metal Poor Extreme Starburst Galaxies: Novel insights on the escape of ionizing photons

Omkar Bait,[1,2,3]★ Daniel Schaerer,[4,5] Yuri I. Izotov[6] and Biny Sebastian[7]
[1] National Radio Astronomy Observatory, 520 Edgemont Road, Charlottesville, VA 22903, USA
[2] The NSF-Simons AI Institute for Cosmic Origins, USA, 201 E. 24th Street, POB 4.102, Austin, Texas 78712-1229
[3] SKA Observatory, Jodrell Bank, Lower Withington, Macclesfield, SK11 9FT, UK
[4] Observatoire de Genève, Université de Genève, Chemin Pegasi, 1290 Versoix, Switzerland
[5] CNRS, IRAP, 14 Avenue E. Belin, 31400 Toulouse, France
[6] Bogolyubov Institute for Theoretical Physics, 14-b Metrolohichna str, Kyiv 03143, Ukraine
[7] Space Telescope Science Institute, 3700 San Martin Drive, Baltimore, MD 21218, USA

arXiv:2503.17327v2 [astro-ph.GA] 9 Mar 2026

Accepted XXX. Received YYY; in original form ZZZ

ABSTRACT

Recent optical surveys have identified a rare population of low-z ($z \sim 0.01 - 0.06$) extreme star-forming galaxies (xSFGs) characterized by very low metallicity, strong emission lines, extremely high specific star-formation rate, low stellar mass, and strong Ly α emission. Their global properties resemble recently discovered $z > 6$ reionization-era star-forming galaxies. We present new multi-frequency radio continuum (RC) observations of 8 xSFGs using the upgraded Giant Metrewave Radio Telescope (uGMRT) at 1.25 GHz, the Karl G. Jansky Very Large Array (VLA) at 1.5, 3.0, 6.0, 10.0 and 15.0 GHz, along with archival LOw Frequency ARray (LOFAR) data at 150 MHz for several sources. These data allow construction of the radio spectral energy distribution (radio-SED) from $\sim$ 1 GHz (down to 150 MHz for some sources) to 15 GHz, spanning nearly two orders of magnitude in frequency. We find that xSFGs exhibit a flat spectral index between 6 and 15 GHz, while a subset shows spectral turnovers at 0.3 – 3 GHz. Our Bayesian radio-SED modeling indicates that these features are consistent with a high thermal fraction combined with free-free absorption, requiring high emission measures in some systems. By comparing modeled thermal radio emission with observed Hβ line flux density, we find evidence for dust in several xSFGs. Finally, we confirm a previously reported correlation between Lyman continuum escape fraction ($f_{\rm esc}^{\rm LyC}$), ionization state, and radio spectral index, particularly among strong leakers.

Key words: galaxies: starburst – galaxies: dwarf – galaxies: ISM – radio continuum: galaxies – radio continuum: ISM – dark ages, reionization, first stars

1 INTRODUCTION

Identifying the nature of sources (at redshift $z > 6$) that led to the reionization of the Universe remains a matter of intense debate. Numerous studies, both on the observational and simulation side, suggest that low-mass dwarf starburst galaxies are likely the dominant sources of reionization (e.g., Ouchi et al. 2009; Bouwens et al. 2015; Robertson et al. 2015; Atek et al. 2015). With the advent of the James Webb Space Telescope (JWST), rest-frame optical spectroscopic studies of reionization-era galaxies ($z \sim 6 - 8$) have become possible revealing their key physical properties. It is found that these galaxies generally have low stellar masses ($\log M_*/M_\odot \leq 9$), compact size (< 1 kpc), and high specific star-formation rates sSFR of $\sim$ 100 Gyr^{-1} (Schaerer et al. 2022; Rhoads et al. 2023; Williams et al. 2023; Endsley et al. 2023; Fujimoto et al. 2023; Mascia et al. 2024). Several of these galaxies are extremely metal-poor (XMPs), with gas-phase metallicities $12 + \log {\rm O/H} < 8.0$ and have hard ionizing radiation (Jones et al. 2020; Schaerer et al. 2022; Rhoads et al. 2023; Langeroodi et al. 2023; Topping et al. 2024; Saxena et al. 2024; Atek et al. 2024). And importantly, they are found to be strong Ly α emitters (LAEs) and also produce a significant amount of ionizing radiation to easily reionize the Universe (Simmonds et al. 2023, 2024; Saxena et al. 2024; Atek et al. 2024).

Despite these significant advances in our understanding of high-z galaxies, the physical mechanisms responsible for their extreme star-forming properties and high LyC escape responsible for reionization remain poorly understood due to a lack of multi-wavelength studies, which is extremely difficult with the current generation telescopes. Moreover, due to optically thick inter-galactic medium it is extremely difficult to detect LyC escape from high-z galaxies (Inoue et al. 2014). We thus have to rely on the local analogs of such high-z galaxies with similar physical properties, e.g., low-mass, compact sizes, high sSFR, low-metallicity and strong Ly α emission etc. (e.g., Cardamone et al. 2009; Yang et al. 2017; Izotov et al. 2011, 2021b), generally found in the Sloan Digital Sky Survey (SDSS) data. These low-z ($z \sim 0.3$)

★ CosmicAI Fellow (obait@nrao.edu (OB))

© 2026 The Authors

analogs are known to produce a significant amount of LyC photons (Schaerer et al. 2016; Izotov et al. 2021b) and importantly a large fraction of them leak (Borthakur et al. 2014; Izotov et al. 2016a,b, 2018a,b, 2021a). These successes in finding local LyC leakers or emitters (LCEs) have led to the recent systematic study of the Low-z Lyman Continuum Survey (LzLCS; Flury et al. 2022a) which has revealed interesting relations between the LyC escape fraction ($f_{\rm esc}^{\rm LyC}$) and several key galaxy physical properties (Flury et al. 2022b; Saldana-Lopez et al. 2022; Xu et al. 2023; Jaskot et al. 2024; Bait et al. 2024).

Recently, a rare population of extreme star-forming galaxies (xSFGs) were discovered with the SDSS which are very compact XMPs having even lower stellar mass ($\log {\rm M_*/M_\odot} \sim 5-8$), high sSFRs ($\sim 300$ Gyr^{-1}) and high [OIII] λ5007 /[OII] λ3727 ratios; $\rm O_{32} \geq 5$, with several in the range of 20-50 (Izotov et al. 2017b, 2020, 2024; Jaskot et al. 2019; Kouroumpatzakis et al. 2024). They show diverse Ly α properties with several sources showing narrow Ly α peak velocity separation ($V_{\rm sep}$) (Izotov et al. 2020, 2024). Such a narrow $V_{\rm sep}$ suggests that they are also strong LyC leakers based on the tight relation between $V_{\rm sep}$ and $f_{\rm esc}^{\rm LyC}$ (Verhamme et al. 2015; Izotov et al. 2018b). Here we focus on the multi-frequency radio continuum (RC) observations of xSFGs to gain new insights on the physical mechanisms driving their extreme SF and potentially strong $f_{\rm esc}^{\rm LyC}$.

RC emission from galaxies in the megahertz (MHz)- to gigahertz (GHz) frequency range has provided important insights on the star-formation process (Condon 1992). RC emission has been found to be an excellent tracer of extinction-free star-formation rate (SFR) in galaxies (e.g., Murphy et al. 2011, and references therein). The RC emission in normal SF galaxies consists of a combination of a flat thermal emission component (free-free emission with a spectral index of -0.1) and a non-thermal emission component (non-thermal spectral index $\alpha_{\rm nth} \sim -0.8$). The non-thermal component arises from synchrotron emission from cosmic-ray particles (CRs) accelerated by supernova (SNe) under magnetic fields. Thus the non-thermal emission can be used to infer the SNe rate, cosmic-ray (CR) energy distribution and the equipartition magnetic fields. The radio spectral energy distribution (radio-SED) of normal SF galaxies shows a power-law behaviour due to a combination of the thermal and non-thermal component. It is generally found that at $\sim$ 1.4 GHz the non-thermal component is dominant comprising of almost 90% of the emission component (e.g., Niklas et al. 1997; Tabatabaei et al. 2017). Detailed multi-frequency radio-SED analysis of nearby SF galaxies has allowed to constrain the relative fraction of thermal ($\rm f_{1GHz}^{th(SED)}$) and non-thermal emission, and $\alpha_{\rm nth}$ (Tabatabaei et al. 2017) and its dependence on various galaxy physical parameters (e.g., the SFR surface density, magnetic fields etc.). Additionally in luminous and ultraluminous infrared galaxies (ULIRGs), there can be a turnover at lower frequencies in the radio-SED due to free-free absorption (FFA) effects (e.g, Clemens et al. 2010; Galvin et al. 2018). Using a combination of thermal and non-thermal radio emission and FFA model, these studies find a high emission measure (EM) in ULIRGs in the range of $\sim 10^6 - 10^7$ pc cm^{-6} (Clemens et al. 2010; Galvin et al. 2018; Dey et al. 2024).

RC studies of dwarf galaxies have revealed different properties compared to massive SF galaxies. The thermal fraction ($\rm f_{1GHz}^{th(SED)}$) is higher in dwarf galaxies, particularly in blue compact dwarfs (Klein et al. 1991; Deeg et al. 1993; Thuan et al. 2004; Ramya et al. 2011). A radio-SED study of nearby dwarf galaxies from $\sim 0.3 - 24$ GHz have shown that they cannot be described by a single power-law and instead show a cuttoff/break at higher frequencies due to various physical processes related to the lack of CRs (Klein et al. 2018). More relevant to our study here, for example in an extremely metal-poor compact dwarf starburst, SBS 0335-052, the integrated radio-SED shows a strong turnover at GHz frequencies, arising due to FFA with a EM $\sim 2-8\times10^7$ pc cm^{-6} and compact size ($\sim$ 17 pc) (Hunt et al. 2004, hereafter: H04). Such a high EM is more commonly observed in resolved radio studies of ultra dense HII regions comprising of young deeply embedded star clusters (e.g., Kobulnicky & Johnson 1999; Johnson & Kobulnicky 2003). Previous single frequency (at 1.4 GHz and 150 MHz) RC observations of objects similar to xSFGs (e.g., green-peas, blueberries) have found that these systems have lower RC flux than that expected from the standard RC-SFR relation (Chakraborti et al. 2012; Sebastian & Bait 2019; Borkar et al. 2024). However, due to limited frequency coverage it is difficult to discern the exact physical mechanisms responsible for such a suppression. Finally, Bait et al. (2024) in a recent radio follow-up study of a subsample of LzLCS sources found that the $f_{\rm esc}^{\rm LyC}$ (and the $\rm O_{32}$, SFR density) depends on the radio spectral index (specifically measured between 3 – 6 GHz). These results motivate a detailed radio-SED study of LCEs to better understand the physical processes governing these relations.

Here, we present new multi-frequency radio-SED observations of a sample of eight xSFGs selected from Izotov et al. (2020, 2024) and Jaskot et al. (2019). Our multi-frequency RC observations were conducted using the NRAO[1] Karl G. Jansky Very Large Array (VLA) at 6 (C-band), 3 (S-band), and (a subsample) at 1.5 (L-band) GHz. We also combine new observations with the upgraded Giant Metrewave Radio Telescope (uGMRT) at Band-5 (1060 - 1460 MHz) together with archival LOw Frequency ARray (LOFAR) data at 120-168 MHz data using the LOFAR Two-metre Sky Survey Data-Release 2 (LoTSS DR2; Shimwell et al. 2017, 2022).

Our paper is organized as follows. In Section 2 we describe our sample, VLA and uGMRT observation setup, data analysis and RC flux density measurements in different radio bands. In Section 3 we present the observed radio-SED of our sample and model the radio-SEDs using Bayesian methods. We then present the dust attenuation measurement using our radio observations. In Section 4, we discuss, 1) on the lack of non-thermal emission in xSFGs 2) the relationship between $f_{\rm esc}^{\rm LyC}$, $\rm O_{32}$, metallicity, and radio spectral index for xSFGs and 3) the overall implications of our observed radio-SED to better understand the extreme nature of high-z galaxies found using the JWST. We then summarize our main results and conclude in Section 5.

2 DATA

In this section, we describe our sample selection and new VLA observations at multiple observing bands, namely: the S (2 - 4 GHz), C (4 - 8 GHz), X (8 - 12 GHz) and Ku (12-18 GHz) bands. We support these observations with new low frequency data using the uGMRT at Band-5 (1060 - 1460 MHz). We also present archival LOFAR data (120 - 168 MHz) covering most of our sample. We also describe our calibration and imaging strategy.

Table 1. Basic properties of our sample of xSFGs.

Target	RA (deg)	DEC (deg)	z	$12+\log O/H$	$\log M_*/M_\odot$	O_{32}[a]	SFR[b] ($M_\odot$/yr)	Lit. source
J0159+0751	29.96979	+7.86356	0.06105	7.56	8.6	39.0	2.3	Izotov et al. (2020)
J0811+4730	122.96721	+47.50729	0.0444	6.98	5.88	5.9	0.19	Izotov et al. (2024)
J0820+5431	125.08029	+54.52781	0.03851	7.49	6.0	22.0	0.2	Izotov et al. (2020)
J1032+4919	158.23633	+49.32979	0.0442	7.59	6.8	24.0	2.4	Izotov et al. (2020)
J1355+4651	208.85692	+46.86426	0.02811	7.56	5.8	23.0	0.1	Izotov et al. (2020)
J150934+373146	227.39239	+37.52948	0.0325	7.88	8.1	15.1	1.35	Jaskot et al. (2019)
J160810+352809	242.04318	+35.46926	0.0327	7.83	7.5	34.9	0.46	Jaskot et al. (2019)
J2229+2725	337.38829	+27.42378	0.07622	7.08	6.96	53.0	0.68	Izotov et al. (2024)

Notes. The physical properties presented here are taken from the literature values shown in the last column.
[a] $O_{32} \equiv$ [OIII] λ5007 /[OII] λ3727.
[b] The SFR is derived using the dust-corrected H β line using the relation from Kennicutt (1998). For J150934+373146 and J160810+352809 the Hα line was used and the relation from Kennicutt & Evans (2012). See the references (last column) for details.

Table 2. Summary of the new radio observations of xSFGs.

Source ID	VLA Observations		VLA Project ID	GMRT Project ID[a]	LOFAR
	B-Config.	C-Config.			
J0159+0751	S, C	X	23A-138, 24A-103	43_062	– –
J0811+4730	S, C	X, Ku	23A-138, 24A-103	43_062	LoTSS DR2
J0820+5431	S, C	X	23A-138, 24A-103	45_075	LoTSS DR2
J1032+4919	L, S, C	X, Ku	23A-138, 24A-103	43_062	LoTSS DR2
J1355+4651	S, C	X, Ku	23A-138, 24A-103	45_075	LoTSS DR2
J150934+373146	S, C	X, Ku	23A-138, 24A-103	34_123 (from SB19)	LoTSS DR2
J160810+352809	S, C	X, Ku	23A-138, 24A-103	34_123 (from SB19)	LoTSS DR2
J2229+2725	S, C	X, Ku	23A-138, 24A-103	45_075	LoTSS DR2

Notes. [a] All the uGMRT observations used here are performed in Band-5.

2.1 Sample

Our sample is selected from the recently identified sample of xSFGs at low-z, $z \sim 0.01 - 0.06$, from Izotov et al. (2020, 2024) and Jaskot et al. (2019) (see also Yang et al. 2017). All our sources have extremely low-metallicity ($12+\log O/H \sim 6.98 - 7.88$), low stellar mass ($\log(M_*/M_\odot) \sim 5.8 - 8.6$), very high O_{32} ($\gtrsim 15$ to up to ~ 53) and high H β equivalent width (EW(Hβ) $\gtrsim 250$). Table 1 summarizes the basic physical properties of our sample of xSFGs. We observed several of these sources at L-, S- and C-bands using the VLA with the B-configuration (PI: Bait; Project Code: 23A-138 & 24A-103) and at higher frequency bands at X- and Ku with the C-configuration (PI: Bait; Project Code: 24A-103). We also conducted follow-up uGMRT Band-5 observations (PI: Bait, Proposal ID: 43_062 and 45_075) for our sample of xSFGs. Table 2 summarizes the observations in different bands and the corresponding project IDs.

Using these data allows us to study the radio-SED at GHz frequencies for these sources. We thus present a sample of 8 xSFGs which has a seamless RC coverage between $\sim 1 - 12$ GHz (S- to X- band) from the two VLA and uGMRT programs. Except for one source (J0159+0751), all our sources also have Ku-band (12−18 GHz) observations (Project Code: 24A-103). For two sources, J150934+373146 and J160810+352809, we use the published Band-5 data from Sebastian & Bait (2019) (SB19 hereafter). J1032+4919 was also observed with the VLA at L-band ($1 - 2$ GHz; under Project Code: 23A-138). We also present LOFAR 150 MHz data which covers 7 out of the 8 sources from our sample. The various physical properties (e.g., metallicity, O_{32}, V_{sep}, observed and dust extinction corrected H β line flux) of the 8 xSFGs studied here are taken from Izotov et al. (2020, 2024) and Jaskot et al. (2019) and shown in Table 1.

In the next section, we present details on the new RC observations at multiple VLA and uGMRT bands together with archival LOFAR observations. Table 3 provides a brief summary of these observations.

2.2 VLA L-, S-, C-, X- and Ku-band Observations and Data Analysis

We used the default VLA setup for our L-, S-, and C-band continuum observations. For the L- and S-bands we used a total bandwidth of 1 and 2 GHz respectively with a 8-bit sampler. The L-band (S-band) was split into one (two) baseband(s) each comprising of 8×128 MHz subbands. For the C-band we used a total bandwidth of 4 GHz with a 3-bit sampler which was split into two basebands each comprising of 16×128 MHz subbands. For each of these cases, the

[1] The National Radio Astronomy Observatory is a facility of the National Science Foundation operated under cooperative agreement by Associated Universities, Inc.

subbands were further split into 64 channels. All of these observations were performed in the B-configuration. This setup is identical to the previously followed setup for RC observations of the LzLCS sources at L-, S- and C-bands from Bait et al. (2024). We adopted the standard observing strategy used for continuum observations at L-, S- and C-bands which was also followed for the LzLCS sources (see Bait et al. 2024, for details). Briefly, after an initial setup, we observed the flux density scale calibrator (for 3 – 5 mins). We then alternative between the phase calibrator (∼ 1min per cycle) and the target (∼ 5 – 6 mins per cycle). The S- and C-band observations were conducted within a single scheduling block (SB) lasting approximately ∼1 hr. We achieved an on-source integration time of 22 mins each for S- and C-band. For the L-band SBs typically lasted for a duration of ∼1 hr and 40 mins, where we achieved an on-source integration time of ∼ 75 mins.

For the high-frequency X- and Ku-band observations we again used the default VLA setup, with a total bandwidth of 4 GHz and 6 GHz respectively with a 3-bit sampler. The total bandwidth for the X-band (Ku-band) was split in 2 (3) subbands each comprising 16×128 MHz subbands. Here as well each subband was further split into 64 channels. These observations were performed in the C-configuration. After an initial setup, we observed the flux density scale calibrator for approximately 5 mins. For the Ku-band an additional scan of ∼4 mins for pointing calibration was performed, where the phase calibrator was used as a pointing calibrator. We then alternative between the phase calibrator (∼ 2 mins per cycle) and the target (∼ 8 mins per cycle). We achieved an on-source integration time of ∼ 15 mins for both the X- and Ku-band.

For all our VLA data reduction, we used the Common Astronomy Software Applications (CASA) data processing software (McMullin et al. 2007; THE CASA TEAM et al. 2022). We followed a similar data reduction procedure as described in Bait et al. (2024). Briefly, each SB was initially flagged and calibrated using the standard VLA calibration pipeline v6.5.4. We manually inspected the calibrated flux density scale and phase calibrators for each SB. Any leftover RFI and poorly performing antennas were manually flagged. And the VLA pipeline was then re-run.

We then extracted the calibrated target and inspected for any left-over RFI in some spectral windows, which was then further flagged. Then we proceeded with the imaging of these data using CASA TCLEAN. For S- and C-bands, since these were observed in the multi-band mode, we first split the target in S- and C-band before imaging (see Bait et al. 2024)). For all our imaging, CASA TCLEAN was setup to use the multi-term multi-frequency synthesis (mtmfs) algorithm (Rau & Cornwell 2011) where the NTERMS were set to 2 and a ROBUST value of 0.5 was used. The flux density and corresponding error (σ) was then estimated by manually making elliptical regions around each of the target sources using CASA task IMVIEW, and a 2D Gaussian fit was performed using the task IMFIT (see Bait et al. 2024, for more details on this procedure). For one marginally resolved source in our sample, J150934+373146 which is also relatively extended in the optical compared to other xSFGs, the flux density and error was measured using PyBDSF (the Python Blob Detector and Source Finder; Mohan & Rafferty 2015). Table 4 presents the flux density and noise (σ) in each band for the sources in our sample. For non-detections, where sources have a signal-to-noise ratio (S/N) below 3, we present the 3σ upper limits as the flux density. Table 4 also shows the synthesized beam properties (beam major/minor axis and position-angle) from our observations in various bands. Note that for all further analysis on the RC flux density, spectral index and radio-SED analysis we add a 5% calibration error in quadrature (following Bait et al. 2024).

2.3 uGMRT Band-5 Observations and Data Analysis

For the uGMRT Band-5 (1460 - 1060 MHz) observations, we used a total bandwidth of 400 MHz split in 2048 channels, similar to that used in SB19.

The data reduction was carried out using the YARP[2] package. YARP comprises a collection of high-level `Python` recipes to perform flagging, calibration and imaging which are based on various standard CASA tasks at the lowest-level. The different flagging, calibration and imaging recipes can be combined to design custom radio data reduction pipelines/workflows for both continuum and spectral line data. The YARP package was first used for GMRT HI 21-cm spectral-line data reduction in Paudel et al. (2023), and a detailed paper describing the package is in preparation.

Here we use the YARP package with CASA v6.5.5 to design a custom pipeline for our uGMRT Band-5 continuum data reduction. Briefly, in this pipeline the raw uGMRT data initially underwent a round of flagging using the CASA task TFCROP. Here any bad/non-working antennas were also flagged which was manually provided to YARP. This data then underwent 5 rounds of calibration (flux, phase and bandpass) and flagging (which used a combination of CASA tasks TFCROP, RFLAG and CLIP). The calibrated data for phase calibrator, flux density scale calibrator and target was manually inspected for any leftover RFI. We then extracted the calibrated target and self-calibrated the data. Each self-calibration round includes three rounds of phase-only self-calibration and one round of Amplitude and Phase self-calibration. For a few cases, the residual (data - model) was flagged using CASA task RFLAG and the flags were applied to the data before proceeding to another round of self-calibration. This final calibrated data was then used for imaging using the MTMFS algorithm with NTERMS set to 2. For all our new Band-5 observations presented here, we do not detect any emission and thus we present the 3σ upper limits. For two xSFGs, J150934+373146 and J160810+352809, the flux density and noise are taken from SB19. Note that J1032+4919 was also observed by SB19 and was also not detected. Our upper limits for J1032+4919 are consistent with SB19. Table 4 presents the flux properties for our sample.

2.4 Archival LoTSS DR2 data

We also present archival LoTSS (120-168 MHz) DR2 imaging data (Shimwell et al. 2022) for our sample. We download cutouts around each of the sources in our sample using the LoTSS DR2 cutout service [3]. We inspected each image to search for detections. Out of the 7 sources which have LoTSS coverage, we detected emission in only one source, J150934+373146. The flux was estimated using PyBDSF. For the rest of the sources we present the 3σ upper limits (see Table 4).

[2] The current development version of the YARP package can be found here: https://github.com/omkarbait/yarp/
[3] https://lofar-surveys.org/dr2_release.html

Table 3. Brief summary of the observation setup for the new multi-frequency radio observations.

Tel.	Band	Cen. Freq.[a] (GHz)	BW[b] (GHz)	TOS[c] (mins)	Array[d]
uGMRT	Band-5	1.25	0.4	120	Full
VLA	L	1.5	1	75	B
VLA	S[e]	3.0	2	20	B
VLA	C[e]	6.0	4	20	B
VLA	X	10.0	4	15	C
VLA	Ku	15.0	6	15	C

Notes. [a] Central frequency of the observing band.
[b] Total Bandwidth.
[c] Time on source (approximate values).
[d] VLA configuration.
[e] The S- and C-band observations were performed simultaneously in a multi-band mode.

Table 4. Radio Fluxes of xSFG.

Freq. (GHz)	Details[a]	J0159+0751	J0811+4730	J0820+5431	J1032+4919	J1355+4651	J150934+373146	J160810+352809	J2229+2725
1.25	S_ν (μJy)	< 64.5	< 58.2	< 69.3	< 48.3	< 46.2	478 ± 36.9[b]	58 ± 17.0[b]	< 79.8
	$\theta_{maj} \times \theta_{min}$	$2.3'' \times 2.1''$	$2.4'' \times 1.9''$	$5.0'' \times 2.3''$	$2.4'' \times 2.2''$	$4.0'' \times 2.1''$	$3.1'' \times 2.6''$	$7.3'' \times 3.3''$	$3.9'' \times 2.0''$
	P.A.	$56.2°$	$21.1°$	$85.4°$	$7.4°$	$-35.6°$	$-69.7°$	$55.4°$	$44.0°$
1.5	S_ν (μJy)	$--$	$--$	$--$	< 41.1	$--$	$--$	$--$	$--$
	$\theta_{maj} \times \theta_{min}$	$--$	$--$	$--$	$3.8'' \times 3.5''$	$--$	$--$	$--$	$--$
	P.A.	$--$	$--$	$--$	$-40.8°$	$--$	$--$	$--$	$--$
3.0	S_ν (μJy)	< 36.6	< 27.3	< 31.8	68.7 ± 9.6	< 32.7	330.0 ± 39.6	$--$[c]	< 29.7
	$\theta_{maj} \times \theta_{min}$	$3.3'' \times 1.8''$	$2.7'' \times 1.9''$	$2.0'' \times 1.7''$	$2.3'' \times 1.8''$	$1.9'' \times 1.7''$	$6.5'' \times 1.7''$	$2.4'' \times 1.8''$	$2.3'' \times 1.8''$
	P.A.	$55.4°$	$68.5°$	$38.6°$	$-83.8°$	$49.7°$	$59.9°$	$84.3°$	$71.1°$
6.0	S_ν (μJy)	34.6 ± 6.4	< 16.8	< 18.9	61.9 ± 5.7	< 19.8	170.0 ± 15.14	46.45 ± 4.6	< 18.6
	$\theta_{maj} \times \theta_{min}$	$1.6'' \times 1.0''$	$1.5'' \times 1.0''$	$1.2'' \times 0.9''$	$1.2'' \times 1.0''$	$1.1'' \times 0.9''$	$2.4'' \times 1.0''$	$1.1'' \times 1.0''$	$1.1'' \times 1.1''$
	P.A.	$50.0°$	$66.0°$	$42.4°$	$-62.0°$	$43.5°$	$63.6°$	$89.7°$	$57.6°$
10.0	S_ν (μJy)	36.0 ± 6.6	< 18.4	< 39.9	53.9 ± 6.8	31.0 ± 6.6	210.0 ± 12.16	43.5 ± 7.6	< 16.7
	$\theta_{maj} \times \theta_{min}$	$4.4'' \times 1.9''$	$3.4'' \times 1.9''$	$2.8'' \times 1.9''$	$3.9'' \times 1.8''$	$5.5'' \times 1.8''$	$2.0'' \times 1.9''$	$2.1'' \times 1.8''$	$2.7'' \times 1.9''$
	P.A.	$-56.0°$	$79.4°$	$-83.4°$	$-74.6°$	$64.3°$	$41.7°$	$-19.3°$	$-75.8°$
15.0	S_ν (μJy)	$--$	< 17.2	$--$	69.0 ± 5.0	28.3 ± 5.4	180.0 ± 22.42	45.14 ± 6.0	< 13.9
	$\theta_{maj} \times \theta_{min}$	$--$	$1.6'' \times 1.3''$	$--$	$1.4'' \times 1.2''$	$2.0'' \times 1.2''$	$3.1'' \times 1.3''$	$2.5'' \times 1.3''$	$2.9'' \times 1.3''$
	P.A.	$--$	$-70.7°$	$--$	$7.4°$	$89.7°$	$73.1°$	$71.6°$	$67.0°$
0.150	S_ν (μJy)	$--$	< 532.4	< 169.5	< 200.2	< 181.9	400.68 ± 126.6	< 225.8	< 316.0
	$\theta_{maj} \times \theta_{min}$	$--$	$6'' \times 6''$	$6'' \times 6''$	$6'' \times 6''$	$6'' \times 6''$	$6'' \times 6''$	$6'' \times 6''$	$6'' \times 6''$
	P.A.	$--$	$90°$	$90°$	$90°$	$90°$	$90°$	$90°$	$90°$

Notes. Sources with no observations in a specific band are shown with empty values.
[a] Shows the measured flux density (S_ν) and beam parameters for each observing frequency. For non-detections we present the 3σ upper limits on the flux densities.
[b] Flux densities and beam parameters taken from SB19.
[c] The VLA S-band flux density for this source could not be measured due to strong artefacts from a neighbouring bright source.

3 RESULTS

Here we present the observed radio-SEDs of 5 out of 8 xSFGs which show detections in one or more radio bands. These sources span a wide range of radio frequencies from 1.2 GHz (from 150 MHz for J150934+373146) to up to 15 GHz using a combination of VLA, uGMRT, and LOFAR telescopes described in Section 2. We perform a Bayesian SED modelling of these sources to derive various physical parameters. We exclude the three other xSFGs from such an analysis since they do not show detections in any bands and no useful constraints can be derived on the physical parameters from their data.

We find that the observed radio-SEDs shown as blue points and red arrows in Figures 1 - 5 have a flat spectral index between 6-15 GHz for most sources, with some sources (J1032+4919 and J150934+373146) showing evidence for a turnover at lower frequencies. J150934+373146 is the only source in our sample which shows a fairly steep ($\alpha \approx -1.0$) below 6 GHz to up to $\sim$ 1 GHz. Between 1 GHz - 150 MHz range it shows evidence for a turnover (or flattening). The presence of a strong turnover at lower frequencies in the radio spectrum of star-forming galaxies can be a signature of free-free absorption (FFA)[4]. The radio spectrum can show such a turnover at GHz frequencies due to a high emission measure (EM), owing to high ionised gas density (H04). Such physical conditions are typical of xSFGs (Izotov et al. 2020, 2024). SBS 0335-052, a nearby low-metallicity starburst, also shows such a turnover but at a slightly lower frequency of $\sim$ 1.5 GHz, although at higher frequencies it is relatively steeper than in xSFGs from our sample (H04). In general, the radio spectra can be flattened due to a change in the dominant cosmic-ray cooling (Hummel 1991; Chyży et al. 2018), however it cannot explain a complete turnover (positive spectral index) in the radio spectra.

3.1 Radio-SED Models

We particularly, consider two radio-SED models,

- Star-forming galaxy (SFG)-thin: Here the total radio emission (S_ν) is optically thin and comprises of a mix of a single thermal ($S_\nu^{\rm th}$) and non-thermal component ($S_\nu^{\rm nth}$), described as:

$$S_\nu = S_\nu^{\rm th} + S_\nu^{\rm nth} = A_1 \left(\frac{\nu}{\nu_\circ}\right)^{-0.1} + A_2 \left(\frac{\nu}{\nu_\circ}\right)^{\alpha_{\rm nth}}. \quad (1)$$

Here, ν is the observed frequency, $\nu_\circ$ is a reference frequency which is fixed to 1 GHz in all our models, thus $A_1 = S^{\rm th}_{\rm 1GHz}$, and $A_2 = S^{\rm nth}_{\rm 1GHz}$. And $\alpha_{\rm nth}$[5] is the non-thermal spectral index. We then define the thermal fraction derived from the radio-SED at a reference frequency of 1 GHz ($f^{\rm th(SED)}_{\rm 1GHz}$) as $f^{\rm th(SED)}_{\rm 1GHz} = S^{\rm th}_{\rm 1GHz}/S_{\rm 1GHz}$. In the most general case there are three free parameters: a) $S^{\rm th}_{\rm 1GHz}$, b) $S^{\rm nth}_{\rm 1GHz}$ and c) $\alpha_{\rm nth}$.

- SFG-thick Model: Here the radio-SED is optically thick and thus shows an additional strong turnover at lower frequencies due to the effect of FFA arising due to high EM in the ISM. Following Galvin et al. (2018); Clemens et al. (2010); Condon (1992), we describe the SFG-thick SED as:

$$S_\nu = \left(1 - \exp\left(-\tau_\nu^{\rm ff}\right)\right)\left(A_1 + A_2\left(\frac{\nu}{\nu_{\rm t}}\right)^{0.1+\alpha_{\rm nth}}\right)\left(\frac{\nu}{\nu_{\rm t}}\right)^2 \quad (2)$$

Here the optical depth ($\tau_\nu^{\rm ff}$) is parametrized using the turnover frequency ($\nu_{\rm t}$) as $\tau_\nu^{\rm ff} = (\nu/\nu_{\rm t})^{-2.1}$. Thus, $\nu_{\rm t}$ is the frequency at which the optical depth becomes 1 (see e.g., Hunt et al. 2004; Clemens et al. 2010; Galvin et al. 2018). In the most general case the free parameters in this model are: a) A_1, b) A_2, c) $\nu_{\rm t}$ and d) $\alpha_{\rm nth}$. By constraining $\nu_{\rm t}$, we can then derive the EM as it is directly related to $\tau_\nu^{\rm ff}$, such that increasing the EM leads to a higher value of $\tau_\nu^{\rm ff}$ (and also of $\nu_{\rm t}$). Specifically, in this work we used the relation from H04 (their Eq. 1) to derive the EM.

3.2 Bayesian model fitting procedure

We incorporate a Bayesian model fitting approach to constrain the thermal/non-thermal emission and to determine the presence of FFA component. We constrain the free parameters in our radio-SEDs using Markov Chain Monte Carlo (MCMC) using the EMCEE package (Foreman-Mackey et al. 2013). We use all the bands in which we have obtained the flux densities together with their observational uncertainities. We also incorporate upper limits on those bands in which we have non-detections. Thus our likelihood function has a mixed form consisting of a term for bands with detection and those with non-detections using the approach derived in Sawicki (2012). This approach is routinely applied in popular SED fitting tools (e.g., CIGALE) to properly treat upper limits (Boquien et al. 2019; Drouart & Falkendal 2018).

We thus construct our log likelihood function, following the derivation in Sawicki (2012) and Drouart & Falkendal (2018), as

$$\ln \mathcal{L}(\theta) = \sum_{\nu_{\rm det}} \left(\frac{S^{\rm obs}_{\nu_{\rm det}} - S^{\rm model}_{\nu_{\rm det}}(\theta)}{\sigma_{\nu_{\rm det}}}\right)^2 - 2\sum_{\nu_{\rm nondet}} \ln\left\{\sqrt{\frac{\pi}{2}}\,\sigma_{\nu_{\rm nondet}}\left[1 + {\rm erf}\left(\frac{S^{\rm lim}_{\nu_{\rm nondet}} - S^{\rm model}_{\nu_{\rm nondet}}(\theta)}{\sqrt{2}\,\sigma_{\nu_{\rm nondet}}}\right)\right]\right\}. \quad (3)$$

Here $S^{\rm obs}_\nu$ and $S^{\rm model}_\nu$ represent the observed and model flux density respectively at a fixed band with detection ($\nu_{\rm det}$) and non-detection ($\nu_{\rm nondet}$). The noise in the detected and non-detected bands is represented by $\sigma_{\rm det}$ and $\sigma_{\rm nondet}$ respectively. The free parameters in the model are represented by θ. The $S^{\rm lim}_{\nu_{\rm nondet}}$ in the error function (erf) represents the value of the upper limit on the flux density generally set to 1σ (Sawicki 2012). For all our model fits, we run the MCMC with 50 walkers for 10,000 steps. We discard the first 200 steps for burn-in and thin them by a factor of 15. Table 5 provides additional information on the Bayesian fitting for individual sources, particularly the choice of priors on the parameters and the radio bands used for fitting.

3.2.1 *Choice of priors*

We adopt uniform priors on $S^{\rm nth}_{\rm 1GHz}$ in a wide range for all our fits (see Table 5) with the lower bound close to zero to maintain positivity. For $S^{\rm th}_{\rm 1GHz}$ we show the fitting results with uniform priors in the same range as $S^{\rm nth}_{\rm 1GHz}$ and also with Gaussian priors. The centre and widths of the Gaussian priors on $S^{\rm th}_{\rm 1GHz}$ were adopted from the

[4] Synchrotron self-absorption (SSA) can also lead to low-frequency turnovers. However, the brightness temperature (T_b) of our sources is too small ($\leq$ 100 K) for SSA to be significant at GHz frequency range, which will require an extremely high $T_b \approx 10^{12}$ K (Condon & Ransom 2016).

[5] In the following, we use this sign convention to define the spectral index. Note that some references use the opposite sign convention.

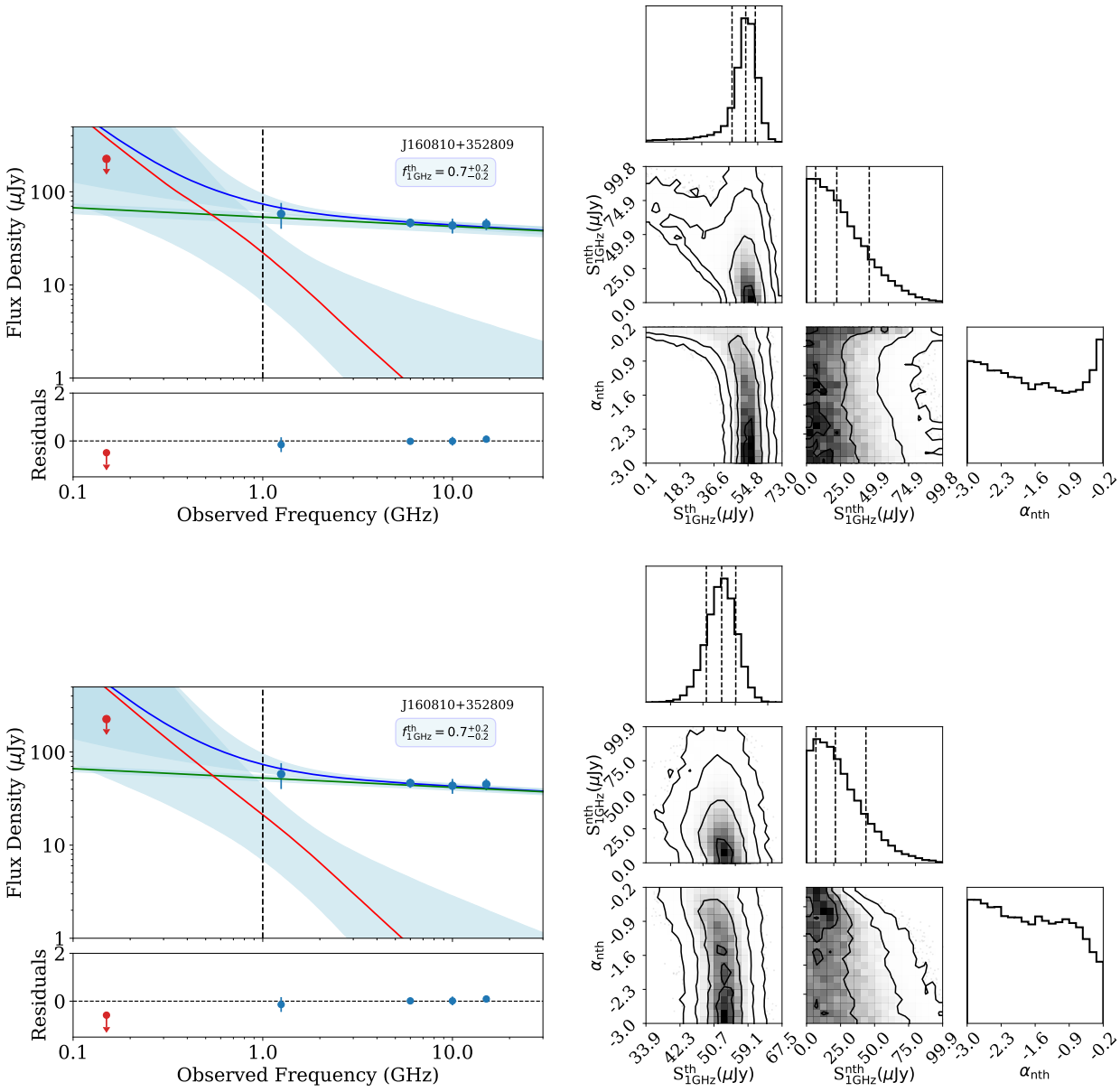

Figure 1. Bayesian radio-SED fitting results for J160810+352809 using the SFG-thin model. Top (bottom) row shows the fitting with flat (Gaussian) priors on S^{th}_{1GHz}. The left panels shows RC detections with blue error bars (wth 1σ errors), and non-detections (3σ upper limits) are shown in red arrows. The corresponding best-fit (median) SFG-thin model is shown in solid blue line. The thermal (non-thermal) components are shown in green (red) solid line. The shaded area shows the 16th and 84th percentile range derived from the MCMC samples. We show the fraction residuals ((data - best-fit model)/best-fit model) in the lower subplot in the left column. The right column shows the 2D and 1D marginalized posteriors on S^{th}_{1GHz}, S^{nth}_{1GHz} and α_{nth} derived from the MCMC chains. The contours enclose 19.3%, 68%, 95% and 99.7% of the 2D marginalized posterior probability. The dashed lines on the 1D marginalized posteriors show the 16th, 50th (median) and 84th percentiles. See Section 3.3 and Table 5 for details on the priors, choice of model and the bands used for the Bayesian fitting. Table 6 summarizes the constraints on the various parameters and constraints on $f^{th(SED)}_{1GHz}$.

physically motivated dust-corrected H β flux density. In Appendix A we describe our procedure of relating the dust-corrected H β flux density and S^{th}_{1GHz}. Further, we provide uniform priors on α_{nth} for all our fits in a wide range of $-3.0 < \alpha_{nth} < -0.2$. The choice of extending the prior on α_{nth} to a very flat value of -0.2 is because in star-forming galaxies α_{nth} is found to flatten with increasing Σ_{SFR} and sSFR (e.g., Tabatabaei et al. 2017, 2025; Basu et al. 2015). The flattening of α_{nth} is due to a more energetic population of CRs in starburst galaxies. xSFGs are known to posses high Σ_{SFR} and sSFR and thus we extend the range of the prior on α_{nth} to such a flat value. Additionally, in compact starburst galaxies with a high ISM gas density ionization and bremsstrahlung losses can be significant and flatter α_{nth} at GHz frequencies than that expected from merely synchrotron losses (Thompson et al. 2006; Murphy 2009; Lacki et al. 2010). In the two cases, where we attempt a modelling with SFG-thick model, we also provide uniform priors on ν_t in a wide range.

The details on the Bayesian modelling with different priors and the radio bands used for fitting is summarized in Table 5.

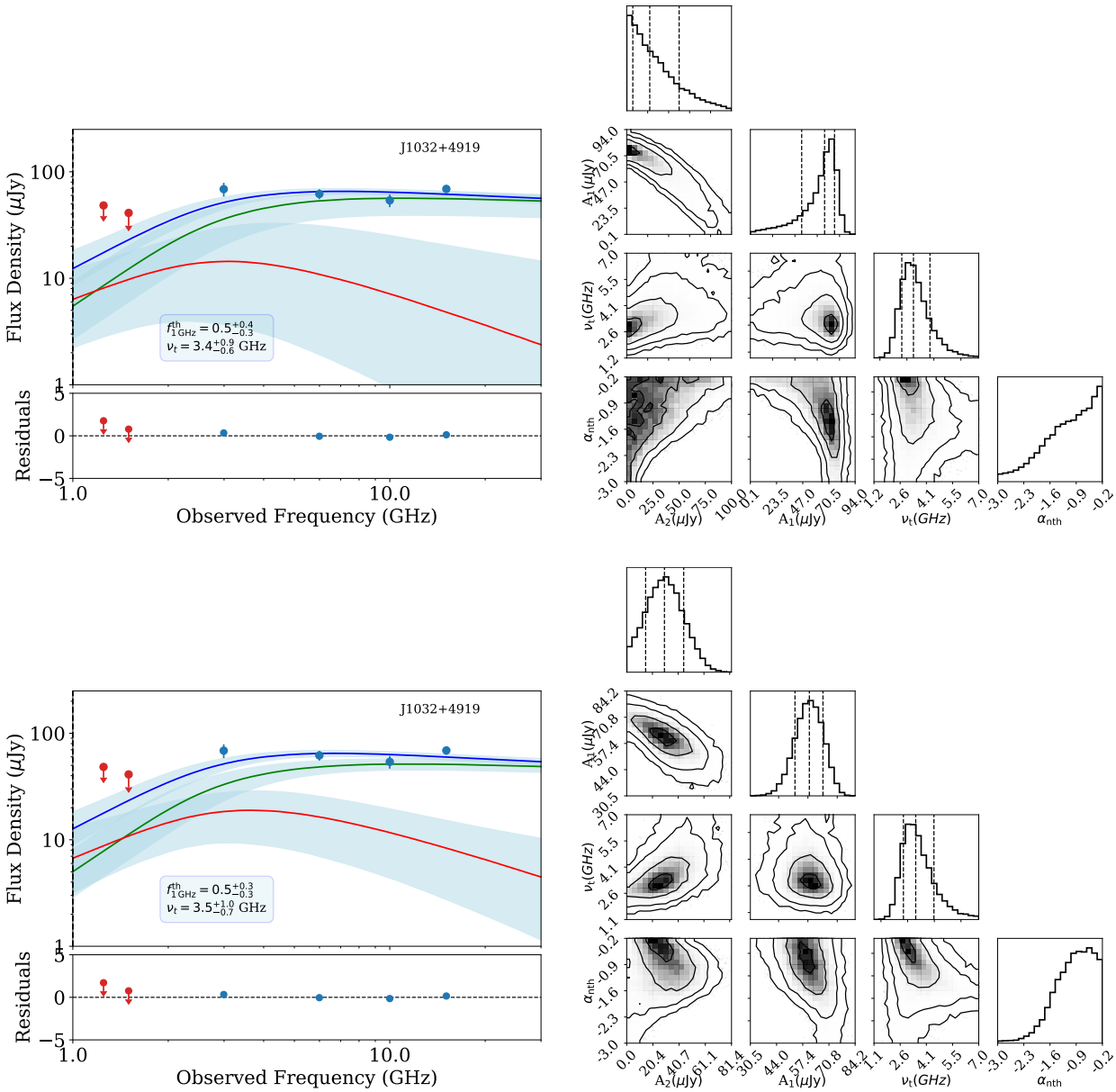

Figure 2. Bayesian radio-SED fitting results for J1032+4919 using the SFG-thick model. The various panels follow the same order as Figure 1 in terms of the choice of priors on S^{th}_{1GHz}. We constrain the ν_t to $\sim$ 3GHz across the different choice of priors (Table 6). Overall we find that the radio-SED is well fit with a thermally dominant SFG-thick radio-SED with a turnover at $\sim$ 3 GHz. See Section 3.3 for a detailed discussion on this source.

3.3 Modelling individual cases

Here we model the individual sources with different radio-SED using a Bayesian approach which allows us to investigate the various degeneracies in the parameters and robustly estimate the thermal/non-thermal component and the dervied physical parameters (e.g., $f^{th(SED)}_{1GHz}$ and EM).

3.3.1 J160810+352809

As seen in Figure 1, this source has a flat radio spectrum from 1.2 – 15 GHz, and can thus be modelled using a SFG-thin radio-SED. We have detections in 4 bands and a non-detection in one LOFAR band for this source. We show the results of the Bayesian fitting using two combinations of priors on S^{th}_{1GHz}:(i) uniform prior in the range of 10^{-6} – 100 μJy (see top row in Figure 1) and (ii) Gaussian priors with the centre and width adopted from the dust-corrected H β flux density (see bottom row in Figure 1). The left column in Figure 1 shows the corresponding best-fit median (50th percentile) SFG-thin model in solid blue line. The individual contribution from the median thermal and non-thermal emission are shown in solid green and red line, respectively. The shaded region shows the 16th and 84th percentile range from the MCMC posterior samples. We also show the fractional residuals between the observed data and the median model for bands with detections and with red upper limits for non-detections in the left panels. The right column in Figure 1 shows the posteriors for S^{th}_{1GHz}, S^{nth}_{1GHz} and α_{nth} and the corresponding 1D marginalized posterior distribution for the two cases of priors.

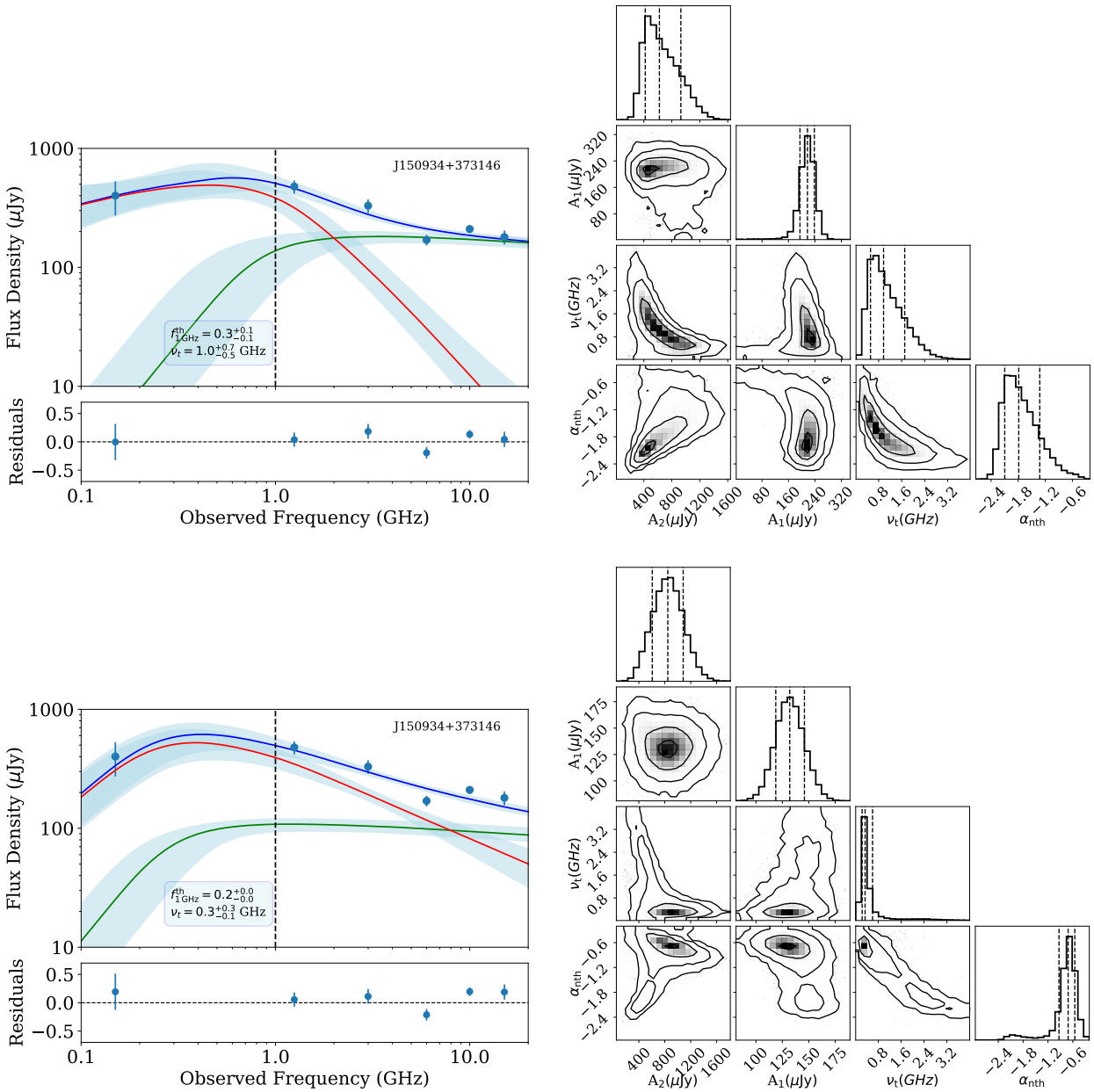

Figure 3. Bayesian radio-SED fitting results for J150934+373146 using the SFG-thick model. The various panels follow the same order as Figure 2 in terms of the choice of priors on S^{th}_{1GHz}. We constrain the ν_t to $\sim 0.34 - 0.39$ GHz across the different choice of priors (Table 6). The radio-SED is well fit with a non-thermally dominant SFG-thick radio-SED typical of normal star-forming galaxies and unlike other xSFGs from our sample. See Section 3.3 for a detailed discussion on this source.

Here the dashed vertical lines show the 16th, 50th (median) and 84th percentiles for the 1D marginalized posterior. See Table 5 for the different choices on prior. We find that the SFG-thin model fits well with the observed data with some degeneracy between S^{th}_{1GHz} and S^{nth}_{1GHz}. Using Gaussian priors reduces the degeneracy between these parameters. In both cases due to a lack of detections at low-frequencies (< 1GHz) we are unable to constrain α_{nth}. The median, 16th and 84th percentile values of the fitted parameters for the two cases of priors are shown in Table 6.

Finally, we derive the $f^{th(SED)}_{1GHz}$ and the uncertainities on it based on the MCMC posterior samples. The median (best-fit) value of $f^{th(SED)}_{1GHz}$ is high (~ 0.7) in both cases (Table 6). The uncertainty (1σ) on $f^{th(SED)}_{1GHz}$ is in the range of 0.2 in both cases. Thus overall our Bayesian analysis supports a thermally dominant SFG-thin radio-SED for J160810+352809. To ensure that our constraints on the non-thermal component were not biased by the lower bound on the S^{nth}_{1GHz} prior ($S^{nth}_{1GHz} \gtrsim 10^{-6}\mu$Jy), we performed a statistical validation by re-running the fit with a uniform prior allowing for negative flux values for S^{nth}_{1GHz}, knowing that this spans the unphysical range for the flux densities. The resulting posterior for S^{nth}_{1GHz} was symmetrically centered on zero, thus robustly confirming the non-negligible contribution of the non-thermal component. This validation demonstrates that our original prior does not introduce significant bias and confirms the robustness of the derived thermal dominance.

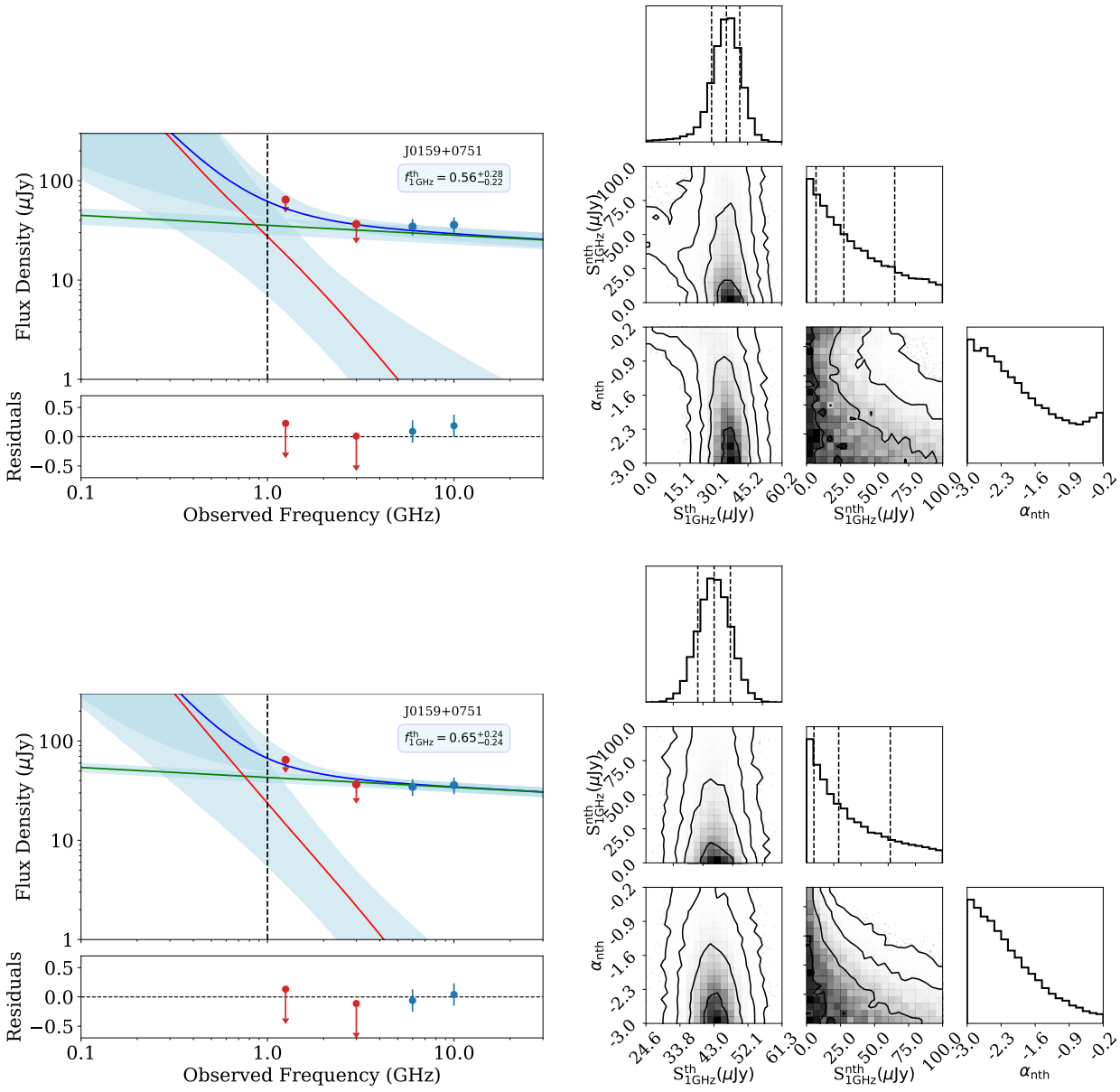

Figure 4. Bayesian radio-SED fitting results for J0159+4919 using the SFG-thin model. The various panels follow the same order followed in Figure 1. See Section 3.3 and Table 5 for details on the priors, choice of model and the bands used for the Bayesian fitting. Table 6 summarizes the constraints on the various parameters and constraints on $f^{th(SED)}_{1GHz}$. We find that the radio-SED is well fit with a thermally dominant component.

3.3.2 J1032+4919

As seen in Figure 2, this source has a flat spectrum at high frequency and the upper limits (3σ) at lower-frequencies suggest a turnover in the radio-SED. The turnover is observed in the uGMRT Band-5 (1.2 GHz) and the VLA L-band (1.5 GHz) both of which are independently observed using two different radio telescopes. A similar level of upper limit was found by Sebastian & Bait (2019) in their independent uGMRT observation (proposal id: 34_123, PI: Sebastian) of this source [6]. Additionally the upper limits shown in red in Figure 2 represent 3σ levels thus increasing the robustness of the turnover. We thus fit this source with the SFG-thick model to better model the turnover in the radio-SED. We follow a similar procedure to the one followed for J160810+352809, and present results of the Bayesian fitting with two different values priors on S^{th}_{1GHz} shown in Figure 2. We let the ν_t to have a uniform prior between 1 – 7 GHz. See Table 5 for details.

We find that the data is well fit with a SFG-thick model for both the choice of priors. In the case of uniform priors on all the parameters there is a strong degeneracy between the thermal, non-thermal component and ν_t. Note that, strictly speaking it appears that the likelihood on the non-thermal component and α_{nth} favours a range beyond our chosen priors. However by choosing hard physical priors we exclude this region of the parameter space due to their unphysical

[6] Additionally the uGMRT data in their study and presented here is reduced using two different radio data reduction pipelines and was based on AIPS in their study and CASA here.

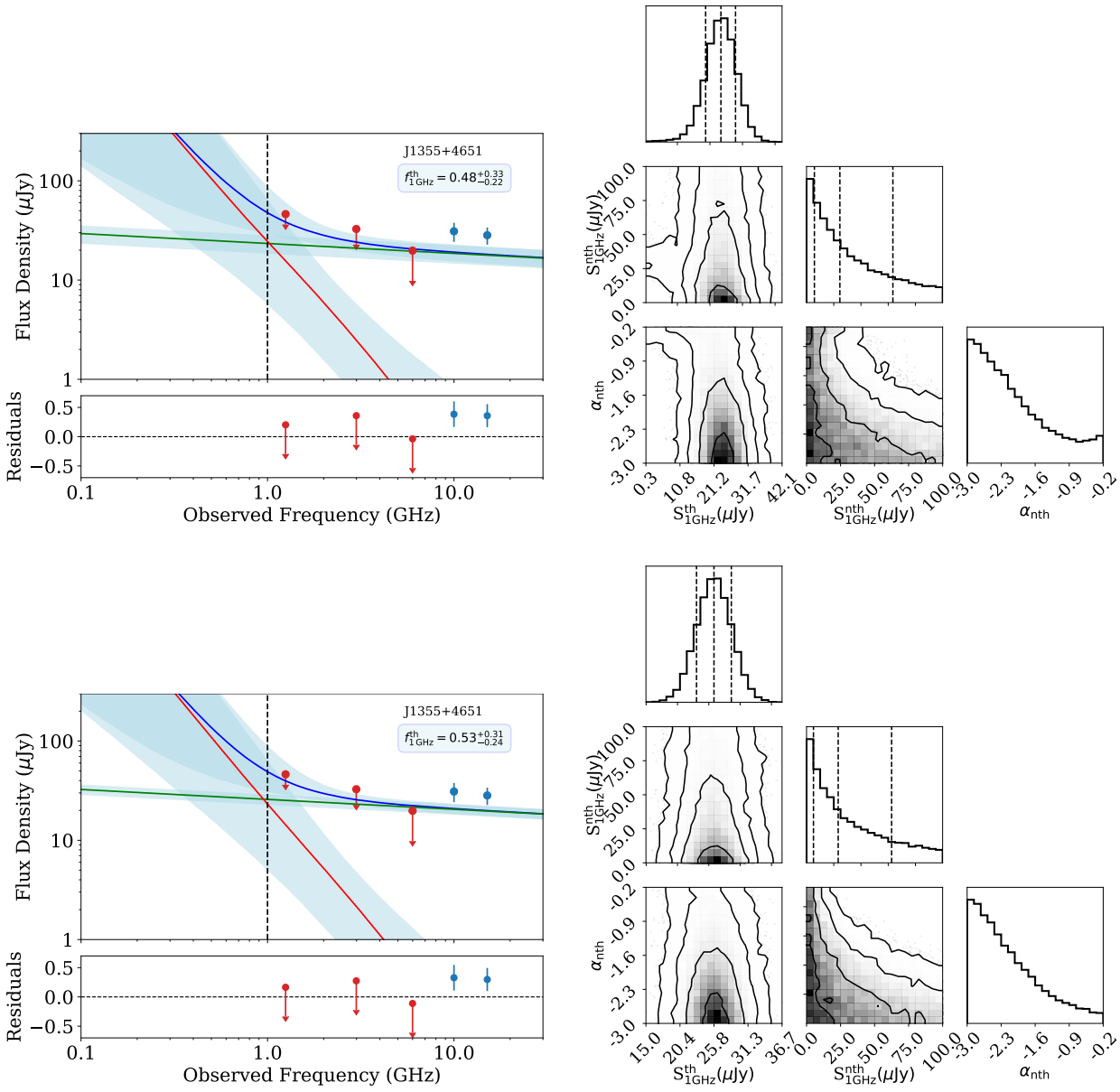

Figure 5. Bayesian radio-SED fitting results for J1355+4651 using the SFG-thin model. The various panels follow the same order as Figure 1 in terms of the choice of priors on S^{th}_{1GHz}. Overall we find that the radio-SED is well fit with a thermally dominant SFG-thin radio-SED. See Section 3.3 for a detailed discussion on this source. We notice weak systematic offset ($< 2\sigma$) in the residuals at 10.0 and 15.0 GHz bands.

nature (see 3.2.1). Using Gaussian priors on S^{th}_{1GHz} informed from the dust-corrected H β flux density helps to reduce this degeneracy. Additionally, the posterior distribution on the non-thermal component is largely within our choice of prior. As shown in Table 6, we are able to well constrain the ν_t to $\sim$ 3.4 GHz (median value) and is consistent within the two choice of priors on S^{th}_{1GHz}. The estimated EM of this source is relatively high $\sim (9-10) \times 10^7$ pc cm^{-6} (see Table 7). Similar to the previous case, α_{nth} remains unconstrained due to lack of detections at low-frequencies. In spite of this, our Bayesian radio-SED analysis favours a thermally dominant SED with the median value (best-fit) of $f^{th(SED)}_{1GHz}$ in the range of $\sim$ 0.5 for both the choice of priors on S^{th}_{1GHz}.

3.3.3 J150934+373146

J150934+373146 has a radio-SED below 10 GHz which is consistent with a steep spectrum and a flattens below $\sim$ 1GHz between the uGMRT Band-5 and LOFAR band. Such a flattening can occur due to the effect of FFA. We thus fit the observed radio-SED with the SFG-thick model following the similar approach as followed for J1032+4919. We choose uniform priors in a wide range for ν_t, S^{nth}_{1GHz} and α_{nth} (see Table 5). In Figure 3 we show the results with flat (top row) and Gaussian (bottom row) priors on S^{th}_{1GHz}. We find that the radio-SED is non-thermally dominant for both the choice of priors, as opposed to the other objects studied in our sample, consistent with its steep apparent spectral index. The median value of $f^{th(SED)}_{1GHz}$ is close to 0.2 – 0.3 close to that typically found in normal star-forming galaxies in the nearby Universe (e.g, Tabatabaei et al. 2017).

Table 5. Details on priors, radio bands and models used for the Bayesian model fitting for each of the source in our sample.

Source	radio-SED Model	Free parameters & Priors	Bands (used for fitting)
J160810+352809	SFG-thin	S^{th}_{1GHz}, S^{nth}_{1GHz}: [10^{-6}, 100] μJy (uniform), α_{nth}: [−3.0, −0.2] (uniform) S^{th}_{1GHz} (Gaussian: 50.8 ± 5.1 μJy), S^{nth}_{1GHz}: [10^{-6}, 100] μJy (uniform), α_{nth}: [−3.0, −0.2] (uniform)	LOFAR, uGMRT (Band-5), VLA (C, X, Ku)
J1032+4919	SFG-thick	S^{th}_{1GHz}, S^{nth}_{1GHz}: [10^{-6}, 100] μJy (uniform), ν_t: [1, 7] GHz (uniform), α_{nth}: [−3.0, −0.2] (uniform) S^{th}_{1GHz} (Gaussian: 57.0±7.4 μJy), S^{nth}_{1GHz}: [10^{-6}, 100] μJy (uniform), ν_t: [1, 7] GHz (uniform), α_{nth}: [−3.0, −0.2] (uniform)	uGMRT (Band-5), VLA (L, S, C, X, Ku)
J150934+373146	SFG-thick	S^{th}_{1GHz}, S^{nth}_{1GHz}: [1, 2000] μJy (uniform), ν_t: [0.1, 7] GHz (uniform), α_{nth}: [−3.0, −0.2] (uniform) S^{th}_{1GHz} (Gaussian: 126.3±12.6 μJy), S^{nth}_{1GHz}: [1, 2000] μJy (uniform), ν_t: [0.1, 7] GHz (uniform), α_{nth}: [−3.0, −0.2] (uniform)	LOFAR, uGMRT (Band-5), VLA (S, C, X, Ku)
J0159+0751	SFG-thin	S^{th}_{1GHz}, S^{nth}_{1GHz}: [10^{-6}, 100] μJy (uniform), α_{nth}: [−3.0, −0.2] (uniform) S^{th}_{1GHz} (Gaussian: 53.1 ± 7.0 μJy), S^{nth}_{1GHz}: [10^{-6}, 100] μJy (uniform), α_{nth}: [−3.0, −0.2] (uniform)	uGMRT (Band-5), VLA (S, C, X)
J1355+4651	SFG-thin	S^{th}_{1GHz}, S^{nth}_{1GHz}: [10^{-6}, 100] μJy (uniform), α_{nth}: [−3.0, −0.2] (uniform) S^{th}_{1GHz} (Gaussian: 27.3 ± 3.6 μJy), S^{nth}_{1GHz}: [10^{-6}, 100] μJy (uniform), α_{nth}: [−3.0, −0.2] (uniform)	uGMRT (Band-5), VLA (S, C, X, Ku)

Table 6. Constrained values of the parameters based on our Bayesian radio SED fitting.

Source	radio-SED Model	S^{th}_{1GHz} (μJy)	S^{nth}_{1GHz} (μJy)	α_{nth} [a]	ν_t (GHz)	$f^{th\,(SED)}_{1GHz}$
J160810+352809	SFG-thin	$53.57^{+5.14}_{-7.33}$	$22.19^{+23.81}_{-15.51}$	−−	−−	$0.70^{+0.19}_{-0.19}$
	SFG-thin (Gaussian prior on S^{th}_{1GHz})	$52.62^{+3.48}_{-3.79}$	$21.20^{+22.41}_{-14.31}$	−−	−−	$0.71^{+0.18}_{-0.17}$
J1032+4919	SFG-thick	$66.62^{+8.90}_{-20.55}$	$21.97^{+28.04}_{-16.15}$	−−	$3.36^{+0.92}_{-0.65}$	$0.51^{+0.36}_{-0.29}$
	SFG-thick (Gaussian prior on S^{th}_{1GHz})	$60.73^{+6.98}_{-7.35}$	$29.30^{+14.97}_{-14.62}$	−−	$3.45^{+1.02}_{-0.69}$	$0.49^{+0.26}_{-0.26}$
J150934+373146	SFG-thick	$217.44^{+20.86}_{-22.64}$	$622.54^{+306.87}_{-202.30}$	$-1.79^{+0.47}_{-0.31}$	$0.97^{+0.73}_{-0.45}$	$0.25^{+0.09}_{-0.10}$
	SFG-thick (Gaussian prior on S^{th}_{1GHz})	$131.97^{+13.92}_{-13.23}$	$847.02^{+237.20}_{-240.09}$	$-0.71^{+0.16}_{-0.22}$	$0.34^{+0.26}_{-0.10}$	$0.19^{+0.03}_{-0.03}$
J0159+0751	SFG-thin	$35.62^{+5.90}_{-6.56}$	$27.42^{+37.37}_{-20.45}$	−−	−−	$0.56^{+0.28}_{-0.22}$
	SFG-thin (Gaussian prior on S^{th}_{1GHz})	$43.00^{+4.37}_{-4.40}$	$23.63^{+37.90}_{-18.19}$	−−	−−	$0.65^{+0.24}_{-0.24}$
J1355+4651	SFG-thin	$23.37^{+4.49}_{-4.70}$	$24.49^{+38.95}_{-18.72}$	−−	−−	$0.48^{+0.33}_{-0.22}$
	SFG-thin (Gaussian prior on S^{th}_{1GHz})	$25.82^{+2.77}_{-2.79}$	$23.25^{+39.25}_{-18.16}$	−−	−−	$0.53^{+0.31}_{-0.24}$

Notes.
Each column reports the median parameter value and the corresponding 16th–84th percentile confidence interval.
[a] For sources with empty values we are unable to contrain the α_{nth} due to lack of detections at low-frequencies.

For this source we are able to constrain the α_{nth}, however there is a degeneracy most strongly between α_{nth}, the non-thermal component and ν_t. In the case of uniform priors on all parameters, our Bayesian model favours a steep α_{nth} of ~ -1.8 and a ν_t close to 1GHz (and an EM of $\sim 0.7 \times 10^7$ pc cm^{-6}). Using Gaussian priors on S^{th}_{1GHz} from the dust-corrected H β line, reduces these degeneracies with well constraints on the thermal and non-thermal component. In this case, we find that a SFG-thick model fits well to the data with an α_{nth} close to the canonical value of −0.7 within the uncertainties, a ν_t at a lower frequency of $\sim$ 0.3 GHz (EM $\sim 8 \times 10^5$ pc cm^{-6}) and $f^{th(SED)}_{1GHz}$ of $\sim$ 0.2. Table 6 provides a fitted values of the paramters for the two choice of priors.

3.4 J0159+0751

As seen in Figure 4, the radio-SED is flat based on the detections at the two high-frequencies bands (> 5GHz) and is consistent with a fairly flat spectrum taking into account the non-detections (3σ upper limits) in the rest of the two bands. We fit the source with a SFG-thin model similar to the case of J160810+352809 (see also Table 5 for choice of priors). Here as well we favour a thermally dominant radio-

SED ($f^{th(SED)}_{1GHz} \sim 0.6$) in the case of both flat and Gaussian priors on S^{th}_{1GHz}. Using Gaussian priors on S^{th}_{1GHz} puts better constraints on the thermal component and somewhat reduces the uncertainties on $f^{th(SED)}_{1GHz}$, thus supporting the thermally dominant radio-SED. The contribution of S^{nth}_{1GHz} (non-thermal component) remains below $\sim$ 62 μJy (84th percentile), however we are unable to put strong lower limits on it. In both the cases we are unable to well constrain α_{nth}, although using Gaussian priors on S^{th}_{1GHz} favours steeper values of α_{nth} based on the 1D posteriors. Similar to the previous case of J1032+4919, it appears that the likelihood on the non-thermal component and α_{nth} favours a range beyond our chosen priors, however we exclude this region on the basis of it being unphysical using hard physical priors. Deeper data at low frequencies will be crucial to better constrain both α_{nth} and S^{nth}_{1GHz} and the nature of the radio-SED at low-frequencies in this case.

3.5 J1355+4651

As seen in Figure 5, the radio-SED is also flat at high-frequencies ($\geq$ 10 GHz) and is also consistent with being flat given the 3σ upper limits on the uGMRT Band-5 (1.2 GHz) and VLA S-band (3 GHz). The upper limit on VLA C-band (6 GHz) suggests that there might be a turnover in the spectrum. For simplicity and lack of strong evidence for a turnover based on the observed data, we attempt for fit this data using the simpler SFG-thin model similar to J0159+0751. We find that the radio-SED is consistent with a thermally dominant SED with $f^{th(SED)}_{1GHz}$ in the range of $\sim$ 0.5. As in the case of J0159+0751, we are unable to well constrain S^{nth}_{1GHz} and α_{nth}, although while using Gaussian priors we prefer $S^{nth}_{1GHz} \leq 63$ μJy (84th percentile) and steeper values of α_{nth}. We notice that there is a very weak offset ($< 2\sigma$) in the residuals at 10.0 and 15.0 GHz in fits with both the versions of the choice of priors on S^{th}_{1GHz}. Similar to the previous case we reject the unphysical region favoured by the likelihood using hard physical priors.Deeper data is required both to increase the significance of detections and to detect in the lower frequencies ($<$ 10.0 GHz) bands to better understand the nature of the radio-SED of this source.

3.6 Comparison between Hβ dust attenuation derived using Balmer lines and RC emission

The radio emission at GHz frequencies is not affected by dust extinction. We can thus use the radio thermal (free-free) emission (S^{th}_{1GHz}) estimated using the radio-SEDs modelling, presented above, to independently derive the expected dust-free H β flux density ($Flux^{Exp}_{H\beta}$). Particularly, we use the S^{th}_{1GHz} derived with uniform priors which provides an independent estimate of the thermal emission using radio data alone. The free-free emission in a galaxy at both the radio and optical wavelengths arise from the same emitting regions. We can then use the ratio between the observed H β (uncorrected for dust) and $Flux^{Exp}_{H\beta}$ to measure the total dust-extinction. In Appendix A, we describe the details on measuring $Flux^{Exp}_{H\beta}$ using S^{th}_{1GHz}. Table 7 shows the derived $Flux^{Exp}_{H\beta}$ for our sample. We use the observed and dust-extinction corrected H β flux densities from Izotov et al. (2020) and Izotov et al. (2024) that are derived from the SDSS spectrum. For J150934+373146 and J160810+352809, we measured the H β line flux density from their SDSS spectrum. We estimated the dust extinction at H β ($A_{H\beta}$) following the procedure described in Izotov et al. (2016c)[7], where we use the V-band extinction (A_V) from Jaskot et al. (2019) and assume a R_V of 2.7 (Izotov et al. 2017a).

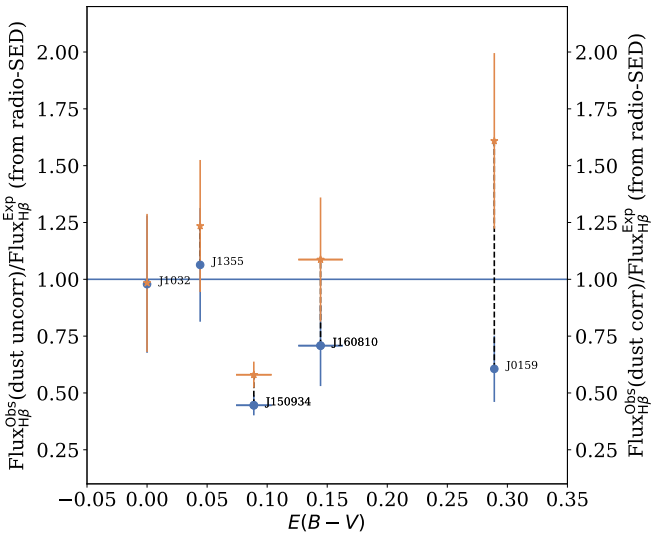

Figure 6. Left-axis: Ratio of the observed H β flux density (dust uncorrected) to that expected from S^{th}_{1GHz} (derived from the radio-SED assuming uniform priors) vs. *E(B-V)* shown in circles. Right-axis: Same as left axis except that the observed H β flux density is corrected for dust, shown in stars. The dashed line connects the points with and without dust correction. Overall we find that in spite of correcting the H β flux density for dust extinction using hydrogen Balmer decrement, in a few cases (e.g., J150934+373146, J160810+352809 and J0159+0751) it is possible that a small fraction ($\sim$ 20 – 30%) of the ionizing radiation emitted by the galaxy is not visible in the Balmer lines. See Sec. 3.6 for a detailed discussion and caveats.

In Figure 6 (left-axis), we compare this ratio against *E(B-V)*[8] shown in blue circles. In the right-axis of Figure 6, we compare the ratio between the dust-corrected H β flux density, derived using hydrogen Balmer decrement, and $Flux^{Exp}_{H\beta}$ with *E(B-V)* shown in stars. Using such a ratio we can compare if the dust correction applied to the observed H β line is completely accounted for by the Balmer decrement. For the cases when this ratio is below 1, we can interpret this as evidence of a fraction of ionizing radiation emitted by the galaxy being missed in the Balmer lines. Note that for a few sources the uncertainties of *E(B-V)* are too small and are not apparent on the figure.

From Figure 6 (left-axis), we find that many sources in our sample show evidence of dust attenuation at optical wavelengths (e.g., in J150934+373146, J160810+352809 and J0159+0751). It is intriguing to find the presence of dust in such low-mass and low-metallicity systems. For J1032+4919 and J1355+4651 this ratio is consistent with 1 within the uncertainities thus suggesting a lack of dust attenuation in these systems. We notice from the right-axis in Figure 6 that after dust-correction from the Balmer decrement to the H β line, the flux density is consistent with $Flux^{Exp}_{H\beta}$ for these sources. This suggests that there is no ionizing radiation being missed in the Balmer lines. For J150934+373146 despite the dust-correction from the Balmer decrement to the H β line, it is possible that some ionizing radiation emitted by the galaxy is missing from the Balmer

[7] Here the $A_{H\beta}$ is derived using $C(H\beta)$ which depends on the A_V and R_V. Effectively this assumes the Cardelli et al. (1989) extinction law which is found to be a better fit for such extreme galaxies (Izotov et al. 2017a).
[8] Here *E(B-V)* is derived using the $C(H\beta)$ values from Izotov et al. (2020) and Izotov et al. (2024), and using $C(H\beta) = 1.47 \times E(B\text{-}V)$.

Table 7. Physical properties of xSFGs from our RC observations.

Target	EM[a]	N_e^b	$\mathrm{Flux}_{H\beta}^{Exp}$ [c]	α_{high}^{low} [d]	f_{esc}^{LyC} (indirect)[e]
J0159+0751	−−	660 ± 300	61.72 ± 14.73	$0.078^{C}_{X} \pm 0.528$	0.091 ± 0.03
J1032+4919	$9.60^{+6.36}_{-3.49}$ ($10.15^{+7.34}_{-3.80}$)	560 ± 50	111.38 ± 34.33	$-0.150^{S}_{C} \pm 0.262$	−−
J1355+4651	−−	1200 ± 150	41.47 ± 9.70	$-0.222^{X}_{Ku} \pm 0.716$	0.169 ± 0.03
J150934+373146	$0.73^{+1.64}_{-0.53}$ ($0.08^{+0.20}_{-0.04}$)		412.96 ± 41.0	$-0.958^{S}_{C} \pm 0.239$	0.034 ± 0.01
J160810+352809	−−		88.70 ± 22.29	$-0.128^{C}_{X} \pm 0.416$	0.31 ± 0.13

Notes. [a] In units of $10^7 \times$ pc cm^{-6}. Values in the bracket are with Gaussian priors on the S^{th}_{1GHz}.
Here we use the T_e values from Izotov et al. (2020) and Izotov et al. (2024) .
For J150934+373146 and J160810+352809 we use a fixed value of 2×10^4K.
[b] In units of cm^{-3}. Values are taken from Izotov et al. (2020, 2024).
[c] Values shown are in units of 10^{-16} ergs/s/cm^2. Derived using S^{th}_{1GHz} from the radio-SED modelling.
[d] The VLA bands used to derive α_{high}^{low} is shown around each value.
[e] f_{esc}^{LyC} values taken from Izotov et al. (2020, 2024) which are indirectly estimated using V_{sep} (Izotov et al. 2018b).

lines. However, J150934+373146 has an extended structure, thus we could be missing some H β flux from the SDSS spectrum. This can reduce the fraction of missing ionizing emission in the Balmer lines than our estimate. J0159+0751 has the highest *E(B-V)* value in our sample and the ratio between the observed H β and $\mathrm{Flux}_{H\beta}^{Exp}$ flux is also relatively low. Notably, after dust-correcting the H β line, the flux density is higher than $\mathrm{Flux}_{H\beta}^{Exp}$, however this discrepancy is only weakly significant within the current uncertainties. Future high-sensitivity and high-frequency observations will be essential to unambiguously confirm the presence of dust in these systems.

Overall, by comparing the independently derived thermal flux density using radio data alone with the dust uncorrected and corrected H β flux density we find evidence for the presence of dust in a few xSFGs despite being very low-mass and extremely metal-poor systems.

4 DISCUSSION

4.1 RC suppression in xSFGs at low frequencies

In Figure 7, we plot the observed RC luminosity at 3 GHz against the SFRs for our sample of xSFGs. Our SFRs are taken from the literature (see Table 1) and are derived using the dust-corrected H β and Hα line luminosity following the (Kennicutt 1998; Kennicutt & Evans 2012) relation. For reference, we overplot the RC (total)-SFR relation at 3 GHz for star-forming galaxies from Murphy et al. (2011, Eq. 15) assuming a α_{nth} of -0.8, shown in solid black line. The thermal RC (RC_{th}) - SFR relation from Murphy et al. (2011, Eq. 11) is shown in solid red line. Note that for J160810+352809, since we were unable to measure the flux density at 3 GHz (see Table 4), we have used the modelled RC flux density at 3 GHz from Section 3.3 and a noise level of 10 μJy typically achieved at S-band for our observations. We note that all our xSFGs show suppressed RC emission than that expected from the RC-SFR relation at 3 GHz, with a few sources even below the RC_{th} - SFR relation. We notice a similar trend in our data at 1.25 GHz using the uGMRT data.

Previous single band radio studies of xSFGs at low-frequencies

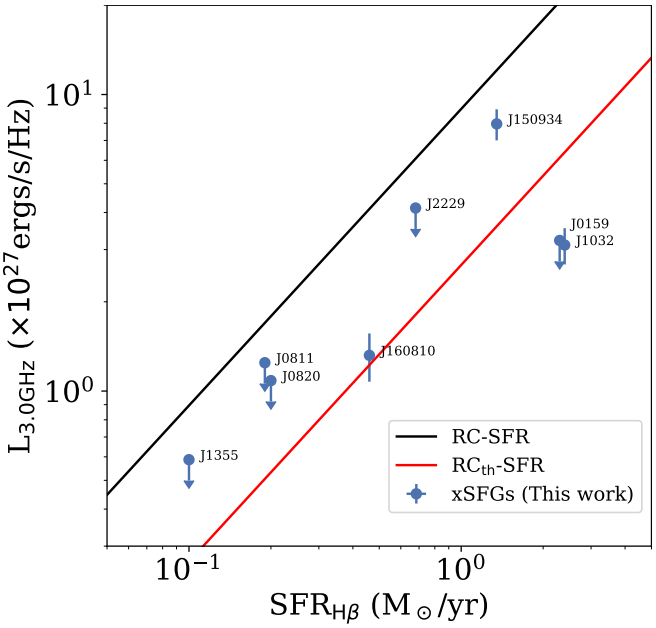

Figure 7. xSFGs on the RC-SFR relation at 3 GHz. We show the standard total RC-SFR relation (Murphy et al. 2011) using a $\alpha_{nth} = -0.8$ with a solid black line. We also show the RC_{th}-SFR relation with a red solid line. In both these cases we have used a fixed value of $T_e = 20000$ K. Our xSFGs show a significant suppression of RC emission than that expected from the total RC-SFR relation. See Section 4.1 for a discussion.

(150 MHz and $\sim$ 1.5 GHz) had also found that the RC emission in such galaxies is suppressed (Chakraborti et al. 2012; Sebastian & Bait 2019; Borkar et al. 2024), which was indirectly associated with a lack of non-thermal emission. Our finding of a thermally dominant radio-SED of xSFGs provides strong evidence for the prevalence of such a scenario. Morevoer the effect of FFA at GHz frequencies could further suppress the RC emission. For example, the RC emission in J1032+4919 was found by SB19 to be highly suppressed at 1.2 GHz compared to other sources in their sample and was the only

undetected source in their study. Our radio-SED observation suggests that this non-detection could be due to FFA at ∼ 3.2 GHz. In some systems RC emission can get suppressed due to FFA even in the presence of non-thermal emission (e.g., in J150934+373146).

In general, there are several scenarios which can lead to a lack of non-thermal emission: 1) extremely young ages (< 5 Myrs) which lack enough SNe (e.g, Hayes et al. 2007; Carilli et al. 2008; Chakraborti et al. 2012; Greis et al. 2017; Sebastian & Bait 2019), 2) ionization and bremsstrahlung losses in compact starburst (Murphy 2009) 3) CR escape (Lisenfeld et al. 2004; Murphy 2009; Sebastian & Bait 2019), 4) strong synchrotron losses due to enhanced magnetic fields (Chakraborti et al. 2012) and 5) Inverse Compton (IC) losses due to high photon density (Condon 1992; Murphy 2009). The young ages of these galaxies are probably the primary reason for the flat spectrum as based on the observed strong nebular emission lines (e.g., high EW(Hβ) > 250Å, Izotov et al. 2020, 2024; Jaskot et al. 2019; Yang et al. 2017). Additionaly, as argued by Murphy (2009), energy loss of CRs due to ionization and bremsstrahlung losses could be an important factor in compact starbursts hosting a dense ISM. The rest of the scenarios involving the lack of CRs (e.g., IC/synchrotron losses, CR escape) would lead to a significant break at high frequencies (Klein et al. 2018). We do not observe such a break in the radio-SED of xSFGs in our data, however, even higher frequency data are required to completely rule them out. Indeed, J150934+373146 is an exception having the highest non-thermal fraction, which possibly has a more complex formation scenario due to a merger with another dwarf galaxy as argued by Dutta et al. (2024).

In summary, xSFGs lack a significant amount of non-thermal emission; however, the exact physical mechanism leading to this suppression is yet to be found.

4.2 Dependence of LyC escape fraction on radio spectral index

Bait et al. (2024) using RC observations of a sub-sample of LzLCS sources from Flury et al. (2022a), showed that the radio spectral index measured between the VLA C- and S-bands ($\alpha^{\rm 3GHz}_{\rm 6GHz}$) correlates with the observed $f^{\rm LyC}_{\rm esc}$. We refer to this as the $f^{\rm LyC}_{\rm esc}$-$\alpha^{\rm low}_{\rm high}$ dependence hereon. Here we measure the radio spectral index ($\alpha^{\rm low}_{\rm high}$) for our detection sample of xSFGs and compare it with the indirectly estimated $f^{\rm LyC}_{\rm esc}$ in Figure 8. The $\alpha^{\rm low}_{\rm high}$ for different sources is measured at several GHz frequencies which show detection. In particular, we use X- and C-bands for J0159+0751 and J160810+352809, Ku- and X-bands for J1355+4651, and C- and S-bands for J150934+373146. The $f^{\rm LyC}_{\rm esc}$ is indirectly estimated using the empirical relation between the Ly α velocity peak separation ($V_{\rm sep}$) and $f^{\rm LyC}_{\rm esc}$ from Izotov et al. (2018b) and are taken directly from Izotov et al. (2020, 2024). For J150934+373146 and J160810+352809, we use the $V_{\rm sep}$ values from Jaskot et al. (2019) to estimate the $f^{\rm LyC}_{\rm esc}$. The $f^{\rm LyC}_{\rm esc}$ values for LzLCS sources are taken from Flury et al. (2022a) and Saldana-Lopez et al. (2022) which are measured using the "UV-fit method" from HST/COS observations. And the $\alpha^{\rm low}_{\rm high}$ is measured between the VLA C- and S-bands taken from Bait et al. (2024). We also overplot in Figure 8 two nearby weak leakers, Haro 11 and Tol 1247 - 232 (see Bait et al. 2024, for references). The two horizontal dashed lines split the sources in three broad categories: strong leakers ($f^{\rm LyC}_{\rm esc}$ > 0.1), weak leakers (0.01 < $f^{\rm LyC}_{\rm esc}$ < 0.1), and non-leakers ($f^{\rm LyC}_{\rm esc}$ < 0.01). The vertical dashed line represents the $\alpha^{\rm 3GHz}_{\rm 6GHz}$ for a simple radio-SED (Simple Model) with $f^{\rm th(SED)}_{\rm 1GHz}$ = 0.1 and $\alpha_{\rm nth}$ = −0.8. We generally refer to sources with $\alpha^{\rm low}_{\rm high}$ > −0.64 as flat spectrum and $\alpha^{\rm low}_{\rm high}$ < −0.64 as steep spectrum. Note that for J1355+4651, the data point exactly falls on another strong leaker source from the LzLCS sample.

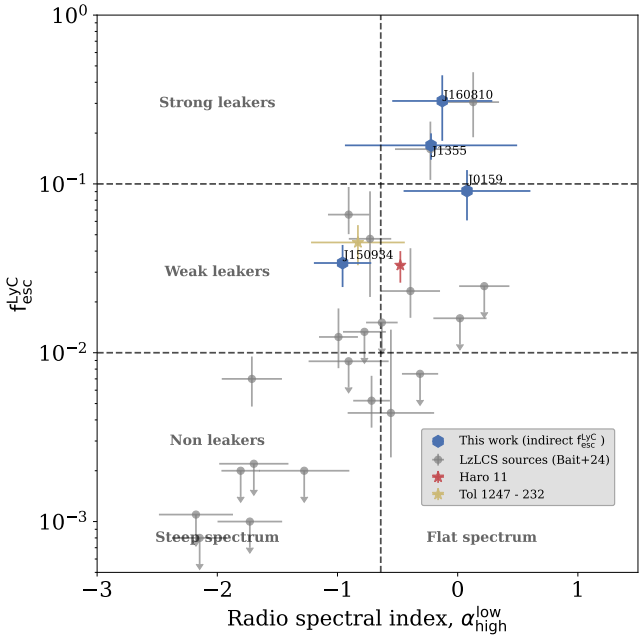

Figure 8. Dependence of $f^{\rm LyC}_{\rm esc}$ on the radio spectral index, $\alpha^{\rm low}_{\rm high}$. xSFGs from this paper are shown in blue hexagons. The sub-sample of sources with VLA RC observations from Bait et al. (2024) are shown in grey circles, along with Haro 11 (red star) and Tol 1247 - 232 (yellow star). Here the $f^{\rm LyC}_{\rm esc}$ is measured directly using the HST/COS observations and the $\alpha^{\rm low}_{\rm high}$ is measured from observations in the C- and S-bands. For our sample of xSFGs the $f^{\rm LyC}_{\rm esc}$ is estimated indirectly using the empirical relation between $V_{\rm sep}$ and $f^{\rm LyC}_{\rm esc}$ from Izotov et al. (2018b). The $\alpha^{\rm low}_{\rm high}$ is measured at GHz frequencies which show a detection (see text for details). The two horizontal dashed lines demarcate the regions termed as strong-, weak- and non-leakers. The vertical dashed line represents $\alpha^{\rm 3GHz}_{\rm 6GHz}$ = −0.64, corresponding to Simple Model, with $f^{\rm th(SED)}_{\rm 1GHz}$ = 0.1 and $\alpha_{\rm nth}$ = −0.8.

Most xSFGs in our sample, except for J150934+373146, are likely strong LyC leakers and possess a flat radio spectrum, as seen in Figure 8. J150934+373146 is the only source which has a steeper radio spectrum and is also a likely weak leaker. Taken together we observe that strong leakers are generally described by a flat radio spectrum at GHz frequencies. On the contrary, not all flat spectrum sources show strong LyC leakage, as we observe a few outliers from the LzLCS sample. Moreover, sources with steep spectrum are either weak- or non-leakers. Quite remarkably that our xSFGs with higher O_{32} values are less metal enriched (see Figure 9 for a comparison between O_{32} and metallicity) and also span a lower stellar mass range ($M_*/M_\odot \leq 10^8$) than LzLCS sources, yet they follow the same $f^{\rm LyC}_{\rm esc}$-$\alpha^{\rm low}_{\rm high}$ dependence. We caution that the $f^{\rm LyC}_{\rm esc}$ for xSFGs is indirectly measured and can be uncertain. Thus, there is tentative evidence that the $f^{\rm LyC}_{\rm esc}$-$\alpha^{\rm low}_{\rm high}$ dependence holds independently of the stellar mass, metallicity and O_{32} ratio for compact star-forming galaxies. Future RC observations particularly focused on strong leakers with direct $f^{\rm LyC}_{\rm esc}$ measurements are required to confirm the universality of the $f^{\rm LyC}_{\rm esc}$-$\alpha^{\rm low}_{\rm high}$ dependence.

Bait et al. (2024) argued that the $f^{\rm LyC}_{\rm esc}$-$\alpha^{\rm low}_{\rm high}$ correlation could be primarily driven by a combination of the age of the starburst and

the density variation of the ISM. Since the radio spectral index is a proxy for the age of the starburst (Cannon & Skillman 2004; Hirashita & Hunt 2006), the youngest starbursts (ages < 5 Myrs) would lack significant non-thermal emission (due to pre-SNe stellar populations) and thus they will have a flat radio spectrum. Additionally, if the source is compact, a large cluster of young stars would be packed in a small region thus boosting the ionized gas density ($N_e \gtrsim 10^3$ cm^{-3}). Since the EM is strongly dependent on N_e [9], this leads to a high EM (in the range of $\sim 10^{7-8}$ pc cm^{-6}, see Hirashita & Hunt 2006, for a detailed model). Such high EMs are typically a sign of a dominance of young massive star clusters (YMCs; see Inoguchi et al. 2024, for a simulation study) in the ISM. Thus the radio free-free emission under such conditions would be optically thick at GHz frequencies (e.g., Johnson & Kobulnicky 2003; Hunt et al. 2004), further leading to a flat/rising radio spectrum associated with a FFA component (see also Hirashita & Hunt 2006; Bait et al. 2024, for a discussion on this).

Based on our study here, we find evidence for such a thermally dominated radio-SED for most of the xSFGs with a couple of systems which are optically thick at GHz frequencies (see Section 3.3). This could suggest that strong leakers possess a dominant population of YMCs in their HII regions. YMCs can boost the star-formation efficiency (SFE; Fall et al. 2010; Menon et al. 2024) thus leading to a paucity of neutral/ molecular gas thus opening channels for LyC photons to escape (Marques-Chaves et al. 2024). Such conditions can thus lead to both efficient production and escape of ionizing photons. Overall, this can explain the flat/rising radio spectrum of strong LyC leakers.

For relatively older starbursts (5 – 10 Myrs), where the radio free-free emission is optically thin and SNe explosions have accelerated the CR electrons producing a significant amount of non-thermal emission, the radio spectra are steeper. Moreover, in a relatively older starburst pressure-driven expansion of the HII region would lead to a lower EM (Hirashita & Hunt 2006), reducing the effect of flattening of the radio spectra due to FFA. Such conditions in the ISM would in general lead to a weaker LyC leakage, as observed in J150934+373146 which has a steep radio spectrum, with a ν_t < 1 GHz and low f_{esc}^{LyC} (< 10%). Finally, Farcy et al. (2022) using radiation-magnetohydrodynamics simulations of disc galaxies find that the CR feedback overall leads to a smooth ISM filling it with denser gas. This overall leads to a lower f_{esc}^{LyC} from galaxies. Thus the mere presence (lack) of CRs in weak/non-leakers (strong leakers) could also drive the f_{esc}^{LyC}-α_{high}^{low} dependence and explain its possible existence over a wide stellar mass range (log $M_*/M_\odot$ = 6 – 11). More work is needed on both the observation and modelling front to understand the exact physical mechanism(s) responsible for the f_{esc}^{LyC}-α_{high}^{low} dependence.

4.3 Relations between α_{high}^{low}, ionization state and metallicity

High values of O_{32} ratio in galaxies could be associated with low-metallicity, high ionization parameter or the presence of density bounded HII regions (Jaskot & Oey 2013; Nakajima & Ouchi 2014). A high O_{32} ratio is found to be a necessary but not a sufficient condition for high f_{esc}^{LyC} in galaxies (Izotov et al. 2018b; Jaskot et al. 2019; Nakajima et al. 2020; Flury et al. 2022b). Thus we investigate if the f_{esc}^{LyC}-α_{high}^{low} dependence could be driven by the dependence of α_{high}^{low} on O_{32} or metallicity.

The dependences between O_{32}-α_{high}^{low} and metallicity-α_{high}^{low} are presented in the left- and right-panel respectively of Figure 9 for xSFGs (in triangles). Such relations were studied by Bait et al. (2024) for a sub-sample of LzLCS sources which are shown in filled circles. This sub-sample lacked sources with very high O_{32}, which is covered by our xSFGs sample. We draw coloured circles around these points differentiating them in three categories: strong- (blue circles), weak- (orange circles) and non-leakers (red circles). Note that although J0159+0751 is classified as a weak-leaker, its f_{esc}^{LyC} indirectly derived from the V_{sep} is $\sim$ 9.1%, thus very close to a strong leaker. Overall, we extend the positive correlation between O_{32} and α_{high}^{low} found by Bait et al. (2024) for the LzLCS sources, to the highest O_{32} ratios (> 10). And indeed as previously found the f_{esc}^{LyC} generally increases with increasing O_{32} ratio (e.g., Izotov et al. 2018b). We also observe several outliers to this trend, wherein the flat spectrum sources have a range of O_{32} (and f_{esc}^{LyC} values). The dependence of metallicity on α_{high}^{low} is not so tight. We do observe that the high metallicity sources from LzLCS have steep spectra (and low f_{esc}^{LyC}), although the flat radio spectrum sources are a mixed population. Thus as previously discussed, not all flat spectrum radio sources have high f_{esc}^{LyC} (or high O_{32}/low-metallicity). Similar to the O_{32} ratio, it appears that a flat radio spectrum is a necessary but not a sufficient condition for strong LyC leakage from galaxies.

Based on the finding that not all high O_{32} ratio sources have high f_{esc}^{LyC}, several studies have suggested that there could be additional physical properties which govern LyC leakage from galaxies, with the viewing angle being a likely possibility (e.g., Izotov et al. 2018b; Jaskot et al. 2019; Nakajima et al. 2020; Katz et al. 2020; Bassett et al. 2019). In our xSFGs, we have such an example of J150934+373146, which has a high O_{32} value (> 10), and low metallicity comparable for instance to J160810+352809. Yet, their f_{esc}^{LyC} values differ by an order of magnitude. However, we notice that their α_{high}^{low} values vary considerably and can be used to predict their indirect f_{esc}^{LyC} values better (see Figure 8). On the other side, we also have sources from the LzLCS sample with low O_{32} that are strong leakers. Here again, such strong leakers have flat α_{high}^{low}. Thus it appears that strong LyC leaking galaxies possess a flatter radio spectrum. Certainly, more data is needed to confirm if α_{high}^{low} could be a primary parameter governing LyC escape in the strongest leakers. If true, this along with the overall correlation between α_{high}^{low} and f_{esc}^{LyC}, and the fact that the α_{high}^{low} is a spatially averaged property could suggest that at least to a first order the orientation might not be a primary driver of f_{esc}^{LyC} (see Bait et al. 2024, for a more detailed discussion).

In summary, estimating f_{esc}^{LyC} from galaxies is a multi-variate problem (e.g., Flury et al. 2022b; Jaskot et al. 2024), and along with the O_{32} ratio, metallicity, dust content and other physical properties, the radio spectral index can play an important role.

4.4 Overall implications from the radio-SED of xSFGs on reionization and high-z galaxies found with JWST

The radio-SED of several xSFGs is found to possess a flat spectral index along with evidence for a turnover at GHz frequencies in a few cases, possibly owing to FFA. These radio-SEDs are akin to those found in ultra-compact and hyper-compact HII regions in our Galaxy (Wood & Churchwell 1989; Yang et al. 2021; Patel et al. 2024).

[9] EM $\propto N_e^2$L, where L is the size of the emitting region, usually in the range of 10-100 pc (Hirashita & Hunt 2006).

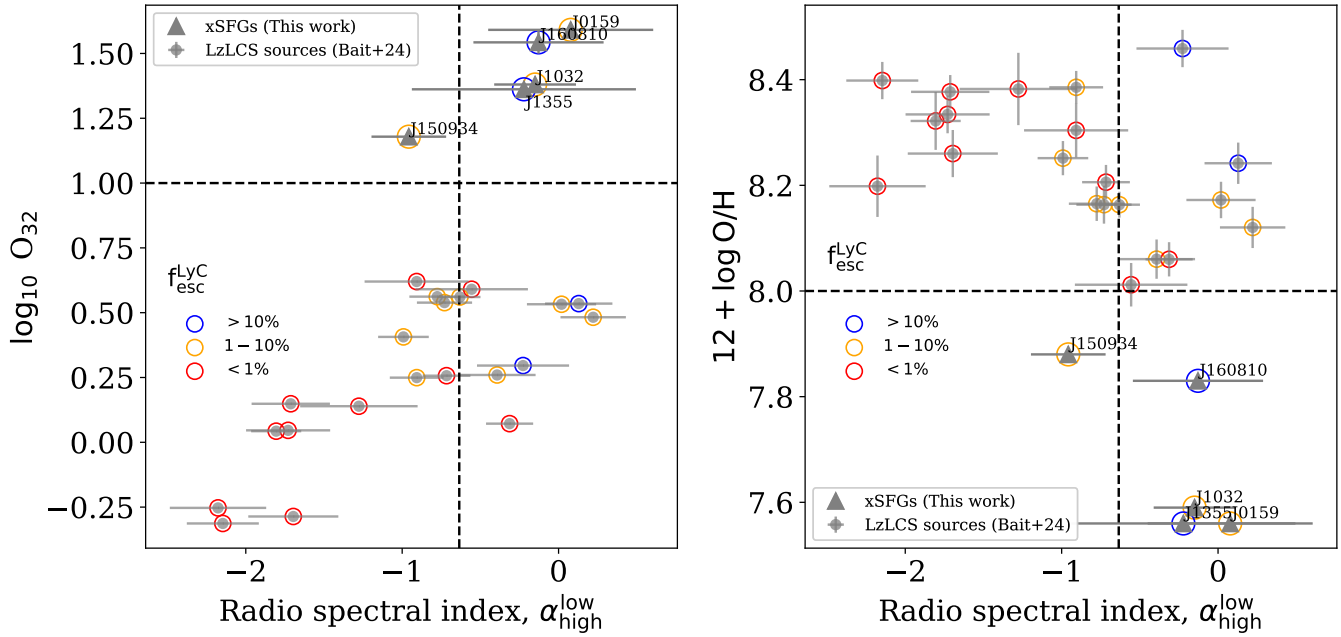

Figure 9. Relations between O_{32} ratio and metallicity (12 + log O/H) with radio spectral index for xSFGs (grey triangles). We show the LzLCS sources with RC measurements from Bait et al. (2024) (grey circles). Around each source we draw circles in blue (f_{esc}^{LyC} > 10%), yellow (f_{esc}^{LyC} = 1 − 10%) and red (f_{esc}^{LyC} < 1%). See Figure 8 and text for details on how the f_{esc}^{LyC} values are derived.

The presence of FFA at GHz frequencies is predicted to be a strong observational signature for the presence of YMCs from simulations (Inoguchi et al. 2024).

Thus our study suggests a picture wherein the extreme star-forming complexes in xSFGs could be dominated by YMC(s) with pre-SNe stellar population. This leads to a high star-formation rate surface density together with a lack of SNe feedback which boosts the star-formation efficiency (SFE) (Fall et al. 2010; Menon et al. 2024) and can explain their extreme star-formation properties (Jecmen & Oey 2023; Marques-Chaves et al. 2024). Such a high SFE can lead to a lack of gas in such galaxies. This can explain the lack of HI detections in low-z green-pea/blueberry galaxies with high O_{32} ratio (Kanekar et al. 2021; Chandola et al. 2024) and the spatial offset between HI and peak of the SF, e.g., in J150934+373146 (Dutta et al. 2024). Together these effects lead to conditions which are suitable for a significant escape of LyC photons (Marques-Chaves et al. 2024; Menon et al. 2024).

Since xSFGs are excellent analogues of high-z galaxies (e.g., Schaerer et al. 2016, 2022; Rhoads et al. 2023), this suggests that the very high-z ($z \geq 6$) galaxies found by JWST might also possess a dominant population of YMCs in their HII regions. Indeed several studies find a dominance of such very dense starclusters in high-z JWST galaxies (Vanzella et al. 2023; Adamo et al. 2024; Messa et al. 2024; Fujimoto et al. 2024). Consequently, these galaxies are expected to be strong LyC leakers and major contributors to reionization.

Finally, our radio-SED study suggests that future deep and ultra-deep radio surveys targeting high-z JWST galaxies with the SKA and ngVLA need to be sensitive to the free-free emission from these galaxies as they are expected to lack a dominant fraction of non-thermal emission.

5 CONCLUSIONS

We present new multi-frequency radio continuum observations of 8 low-z xSFGs using the uGMRT, VLA and archival LOFAR telescope to study their radio-SED. xSFGs are a population of rare metal-poor (12 + log O/H < 8.0), compact starburst galaxies at low-z. Using various indicators they are found to be excellent analogues of high-z ($z > 6$) galaxies found with JWST. We studied and modelled the radio-SED in a wide frequency range from ∼1 to 15 GHz (with a lower limit of 150 MHz for a few sources) using a Bayesian analysis, to gain novel insights on the nature of extreme star-formation properties and the escape of LyC from these galaxies.

We perform a Bayesian modelling of five xSFGs which shows detections in one or more bands, thus allowing us to put useful constraints on the physical parameters. We also incorporate non-detections in the rest of the bands in our Bayesian analysis. Further, to better constrain the parameters, we also show results using priors on the thermal component (S_{1GHz}^{th}) using information from the dust-corrected H β flux density.. Our main results can be summarized as follows:

(i) The radio-SED of three xSFGs (J160810+352809, J0159+0751 and J1355+4651) shows a flat radio spectrum between 6 − 15 GHz. We model these sources using a SFG-thin model composed of a thermal and non-thermal components. Our Bayesian analysis provides evidence for a thermally dominant radio-SED with a $f_{1GHz}^{th(SED)}$ in the range of 0.5 − 0.7. These results remain consistent even when using well-informed priors on S_{1GHz}^{th} from the dust-corrected H β line, thus providing further support for the thermally dominant scenario.

(ii) In the case of J1032+4919, we model the radio-SED using a combined SFG-thick framework, jointly fitting bands with both detections and non-detections. Our Bayesian analysis favors a radio-SED characterized by a high thermal fraction ($f_{1GHz}^{th(SED)} \sim 0.5$), to-

gether with a FFA component corresponding to a large emission measure (EM $\sim (9-10) \times 10^7$ pc cm^{-6}).

(iii) J150934+373146 is the only source in our sample which shows a steep spectrum at high frequencies (> 1 GHz) and a flattening below it. Using a SFG-thick model, our Bayesian modelling with priors on the S^{th}_{1GHz} from the H β flux density suggests that it can be well modelled with an $f^{th(SED)}_{1GHz} \sim 0.2$ and a relatively lower EM of $\sim 8 \times 10^5$ pc cm^{-6}.

(iv) Thermally dominant radio spectra and/or the presence of a FFA component in such systems can explain RC suppression found in previous studies (Sec. 4.1) and their extreme properties (Sec. 4.4).

(v) Using indirect estimates of f^{LyC}_{esc} in xSFGs, we confirmed the relation between α^{3GHz}_{6GHz} and f^{LyC}_{esc} from Bait et al. (2024), particularly for strong leakers (Figure. 8).

(vi) We also extended the previously found empirical relation between α^{3GHz}_{6GHz} and O_{32} ratio to high values of O_{32} (Figure 9).

Future deep low-frequency observations will be crucial to constrain the non-thermal spectral index (α_{nth}) and the amount of subdominant non-thermal component in these systems to better understand the role of SNe feedback in driving the extreme properties of these sources.

ACKNOWLEDGEMENTS

We would like to thank the referee for their useful comments. This work was supported by the National Science Foundation under Cooperative Agreement 2421782 and the Simons Foundation grant MPS-AI-00010515 awarded to the NSF-Simons AI Institute for Cosmic Origins — CosmicAI, https://www.cosmicai.org/. O. Bait (OB) was also supported by the *AstroSignals* Sinergia Project funded by the Swiss National Science Foundation where part of the work was completed. OB would like to thank Heidi Medlin for help with the VLA scheduling. We thank the staff of the GMRT who have made these observations possible. GMRT is run by the National Center for Radio Astrophysics (NCRA) of the Tata Institute of Fundamental Research. OB would also like to thank NCRA for hosting him where part of this work was completed. Y.I. acknowledges support from the National Academy of Sciences of Ukraine (Project No. 0126U000353) and from the Simons Foundation.

LOFAR is the Low Frequency Array designed and constructed by ASTRON. It has observing, data processing, and data storage facilities in several countries, which are owned by various parties (each with their own funding sources), and which are collectively operated by the ILT foundation under a joint scientific policy. The ILT resources have benefited from the following recent major funding sources: CNRS-INSU, Observatoire de Paris and Université d'Orléans, France; BMBF, MIWF-NRW, MPG, Germany; Science Foundation Ireland (SFI), Department of Business, Enterprise and Innovation (DBEI), Ireland; NWO, The Netherlands; The Science and Technology Facilities Council, UK; Ministry of Science and Higher Education, Poland; The Istituto Nazionale di Astrofisica (INAF), Italy.

This research made use of the Dutch national e-infrastructure with support of the SURF Cooperative (e-infra 180169) and the LOFAR e-infra group. The Jülich LOFAR Long Term Archive and the German LOFAR network are both coordinated and operated by the Jülich Supercomputing Centre (JSC), and computing resources on the supercomputer JUWELS at JSC were provided by the Gauss Centre for Supercomputing e.V. (grant CHTB00) through the John von Neumann Institute for Computing (NIC).

This research made use of the University of Hertfordshire high-performance computing facility and the LOFAR-UK computing facility located at the University of Hertfordshire and supported by STFC [ST/P000096/1], and of the Italian LOFAR IT computing infrastructure supported and operated by INAF, and by the Physics Department of Turin university (under an agreement with Consorzio Interuniversitario per la Fisica Spaziale) at the C3S Supercomputing Centre, Italy.

DATA AVAILABILITY

Raw VLA data used in this work are available online in the VLA archive (https://data.nrao.edu/portal/) under project code: 23A-138 & 24A-103. Raw uGMRT data are available in the GMRT Online Archive (http://naps.ncra.tifr.res.in/goa/) under proposal ID: 43_062 and 45_075. LOFAR LoTSS DR2 data used in this work is publicly available at https://lofar-surveys.org/dr2_release.html.

REFERENCES

Adamo A., et al., 2024, Nature, 632, 513
Atek H., et al., 2015, ApJ, 814, 69
Atek H., et al., 2024, Nature, 626, 975
Bait O., et al., 2024, A&A, 688, A198
Bassett R., et al., 2019, MNRAS, 483, 5223
Basu A., Beck R., Schmidt P., Roy S., 2015, MNRAS, 449, 3879
Boquien M., Burgarella D., Roehlly Y., Buat V., Ciesla L., Corre D., Inoue A. K., Salas H., 2019, A&A, 622, A103
Borkar A., et al., 2024, A&A, 687, A137
Borthakur S., Heckman T. M., Leitherer C., Overzier R. A., 2014, Science, 346, 216
Bouwens R. J., Illingworth G. D., Oesch P. A., Caruana J., Holwerda B., Smit R., Wilkins S., 2015, ApJ, 811, 140
Cannon J. M., Skillman E. D., 2004, ApJ, 610, 772
Cardamone C., et al., 2009, MNRAS, 399, 1191
Cardelli J. A., Clayton G. C., Mathis J. S., 1989, ApJ, 345, 245
Carilli C. L., et al., 2008, ApJ, 689, 883
Chakraborti S., Yadav N., Cardamone C., Ray A., 2012, ApJ, 746, L6
Chandola Y., Tsai C.-W., Saikia D. J., Li G., Li D., Ma Y.-Z., 2024, arXiv e-prints, p. arXiv:2411.13527
Chyży K. T., et al., 2018, A&A, 619, A36
Clemens M. S., Scaife A., Vega O., Bressan A., 2010, MNRAS, 405, 887
Condon J. J., 1992, ARA&A, 30, 575
Condon J. J., Ransom S. M., 2016, Essential Radio Astronomy
Deeg H.-J., Brinks E., Duric N., Klein U., Skillman E., 1993, ApJ, 410, 626
Dey S., Goyal A., Małek K., Díaz-Santos T., 2024, ApJ, 966, 61
Drouart G., Falkendal T., 2018, MNRAS, 477, 4981
Dutta S., Bera A., Bait O., Narayan C. A., Sebastian B., Vaddi S., 2024, MNRAS,
Endsley R., Stark D. P., Whitler L., Topping M. W., Chen Z., Plat A., Chisholm J., Charlot S., 2023, MNRAS, 524, 2312
Fall S. M., Krumholz M. R., Matzner C. D., 2010, ApJ, 710, L142
Farcy M., Rosdahl J., Dubois Y., Blaizot J., Martin-Alvarez S., 2022, MNRAS, 513, 5000
Flury S. R., et al., 2022a, ApJS, 260, 1
Flury S. R., et al., 2022b, ApJ, 930, 126
Foreman-Mackey D., Hogg D. W., Lang D., Goodman J., 2013, PASP, 125, 306
Fujimoto S., et al., 2023, ApJ, 949, L25
Fujimoto S., et al., 2024, arXiv e-prints, p. arXiv:2402.18543
Galvin T. J., et al., 2018, MNRAS, 474, 779
Greis S. M. L., Stanway E. R., Levan A. J., Davies L. J. M., Eldridge J. J., 2017, MNRAS, 470, 489

Hayes M., Östlin G., Atek H., Kunth D., Mas-Hesse J. M., Leitherer C., Jiménez-Bailón E., Adamo A., 2007, MNRAS, 382, 1465
Hirashita H., Hunt L. K., 2006, A&A, 460, 67
Hummel E., 1991, A&A, 251, 442
Hunt L. K., Dyer K. K., Thuan T. X., Ulvestad J. S., 2004, ApJ, 606, 853
Inoguchi M., Hosokawa T., Fukushima H., Tanaka K. E. I., Yajima H., Mineshige S., 2024, MNRAS, 527, 3612
Inoue A. K., Shimizu I., Iwata I., Tanaka M., 2014, MNRAS, 442, 1805
Izotov Y. I., Guseva N. G., Thuan T. X., 2011, ApJ, 728, 161
Izotov Y. I., Schaerer D., Thuan T. X., Worseck G., Guseva N. G., Orlitová I., Verhamme A., 2016a, MNRAS, 461, 3683
Izotov Y. I., Guseva N. G., Fricke K. J., Henkel C., 2016b, MNRAS, 462, 4427
Izotov Y. I., Orlitová I., Schaerer D., Thuan T. X., Verhamme A., Guseva N. G., Worseck G., 2016c, Nature, 529, 178
Izotov Y. I., Guseva N. G., Fricke K. J., Henkel C., Schaerer D., 2017a, MNRAS, 467, 4118
Izotov Y. I., Thuan T. X., Guseva N. G., 2017b, MNRAS, 471, 548
Izotov Y. I., Schaerer D., Worseck G., Guseva N. G., Thuan T. X., Verhamme A., Orlitová I., Fricke K. J., 2018a, MNRAS, 474, 4514
Izotov Y. I., Worseck G., Schaerer D., Guseva N. G., Thuan T. X., Fricke Verhamme A., Orlitová I., 2018b, MNRAS, 478, 4851
Izotov Y. I., Schaerer D., Worseck G., Verhamme A., Guseva N. G., Thuan T. X., Orlitová I., Fricke K. J., 2020, MNRAS, 491, 468
Izotov Y. I., Worseck G., Schaerer D., Guseva N. G., Chisholm J., Thuan T. X., Fricke K. J., Verhamme A., 2021a, MNRAS, 503, 1734
Izotov Y. I., Guseva N. G., Fricke K. J., Henkel C., Schaerer D., Thuan T. X., 2021b, A&A, 646, A138
Izotov Y. I., Thuan T. X., Guseva N. G., Schaerer D., Worseck G., Verhamme A., 2024, MNRAS, 527, 281
Jaskot A. E., Oey M. S., 2013, ApJ, 766, 91
Jaskot A. E., Dowd T., Oey M. S., Scarlata C., McKinney J., 2019, ApJ, 885, 96
Jaskot A. E., et al., 2024, arXiv e-prints, p. arXiv:2406.10171
Jecmen M. C., Oey M. S., 2023, ApJ, 958, 149
Johnson K. E., Kobulnicky H. A., 2003, ApJ, 597, 923
Jones T., Sanders R., Roberts-Borsani G., Ellis R. S., Laporte N., Treu T., Harikane Y., 2020, ApJ, 903, 150
Kanekar N., Ghosh T., Rhoads J., Malhotra S., Harish S., Chengalur J. N., Jones K. M., 2021, ApJ, 913, L15
Katz H., et al., 2020, MNRAS, 498, 164
Kennicutt Jr. R. C., 1998, ARA&A, 36, 189
Kennicutt R. C., Evans N. J., 2012, ARA&A, 50, 531
Klein U., Weiland H., Brinks E., 1991, A&A, 246, 323
Klein U., Lisenfeld U., Verley S., 2018, A&A, 611, A55
Kobulnicky H. A., Johnson K. E., 1999, ApJ, 527, 154
Kouroumpatzakis K., et al., 2024, A&A, 688, A159
Lacki B. C., Thompson T. A., Quataert E., 2010, ApJ, 717, 1
Langeroodi D., et al., 2023, ApJ, 957, 39
Lisenfeld U., Wilding T. W., Pooley G. G., Alexander P., 2004, MNRAS, 349, 1335
Marques-Chaves R., et al., 2024, arXiv e-prints, p. arXiv:2407.18804
Mascia S., et al., 2024, A&A, 685, A3
McMullin J. P., Waters B., Schiebel D., Young W., Golap K., 2007, in Astronomical data analysis software and systems XVI. p. 127
Melnick J., Heydari-Malayeri M., Leisy P., 1992, A&A, 253, 16
Menon S. H., Burkhart B., Somerville R. S., Thompson T. A., Sternberg A., 2024, arXiv e-prints, p. arXiv:2408.14591
Messa M., et al., 2024, arXiv e-prints, p. arXiv:2407.20331
Mohan N., Rafferty D., 2015, PyBDSF: Python Blob Detection and Source Finder, Astrophysics Source Code Library, record ascl:1502.007
Murphy E. J., 2009, ApJ, 706, 482
Murphy E. J., et al., 2011, ApJ, 737, 67
Nakajima K., Ouchi M., 2014, MNRAS, 442, 900
Nakajima K., Ellis R. S., Robertson B. E., Tang M., Stark D. P., 2020, ApJ, 889, 161
Niklas S., Klein U., Wielebinski R., 1997, A&A, 322, 19
Ouchi M., et al., 2009, ApJ, 706, 1136
Patel A. L., Urquhart J. S., Yang A. Y., Moore T., Thompson M. A., Menten K. M., Csengeri T., 2024, MNRAS, 533, 2005
Paudel S., Yoon S.-J., Bait O., Sengupta C., Zee W.-B. G., Chhatkuli D. N., Adhikari B., Aryal B., 2023, ApJ, 951, L36
Ramya S., Kantharia N. G., Prabhu T. P., 2011, ApJ, 728, 124
Rau U., Cornwell T. J., 2011, A&A, 532, A71
Rhoads J. E., et al., 2023, ApJ, 942, L14
Robertson B. E., Ellis R. S., Furlanetto S. R., Dunlop J. S., 2015, ApJ, 802, L19
Saldana-Lopez A., et al., 2022, A&A, 663, A59
Sawicki M., 2012, PASP, 124, 1208
Saxena A., et al., 2024, A&A, 684, A84
Schaerer D., Izotov Y. I., Verhamme A., Orlitová I., Thuan T. X., Worseck G., Guseva N. G., 2016, A&A, 591, L8
Schaerer D., Marques-Chaves R., Barrufet L., Oesch P., Izotov Y. I., Naidu R., Guseva N. G., Brammer G., 2022, A&A, 665, L4
Sebastian B., Bait O., 2019, ApJ, 882, L19
Shimwell T. W., et al., 2017, A&A, 598, A104
Shimwell T. W., et al., 2022, A&A, 659, A1
Simmonds C., et al., 2023, MNRAS, 523, 5468
Simmonds C., et al., 2024, arXiv e-prints, p. arXiv:2409.01286
THE CASA TEAM et al., 2022, arXiv e-prints, p. arXiv:2210.02276
Tabatabaei F. S., et al., 2017, ApJ, 836, 185
Tabatabaei F., et al., 2025, arXiv e-prints, p. arXiv:2506.16275
Thompson T. A., Quataert E., Waxman E., Murray N., Martin C. L., 2006, ApJ, 645, 186
Thuan T. X., Hibbard J. E., Lévrier F., 2004, AJ, 128, 617
Topping M. W., et al., 2024, MNRAS, 529, 3301
Vanzella E., et al., 2023, ApJ, 945, 53
Verhamme A., Orlitová I., Schaerer D., Hayes M., 2015, A&A, 578, A7
Williams H., et al., 2023, Science, 380, 416
Wood D. O. S., Churchwell E., 1989, ApJS, 69, 831
Xu X., et al., 2023, ApJ, 943, 94
Yang H., Malhotra S., Rhoads J. E., Wang J., 2017, ApJ, 847, 38
Yang A. Y., et al., 2021, A&A, 645, A110

APPENDIX A: DERIVING THE RADIO-BASED $\mathrm{Flux}^{\mathrm{Exp}}_{\mathrm{H}\beta}$ FLUX DENSITY

We derive the expected H β line flux density from radio ($\mathrm{Flux}^{\mathrm{Exp}}_{\mathrm{H}\beta}$) following H04 (see their Appendix Eq. A10) which relates the radio-derived thermal flux density and the H β line flux density. This relation has been found to be better applicable for low-metallicity HII with high electron temperatures ($> 10,000$ K) which is the case for xSFGs. Here we also assumed a ionized Helium to Hydrogen ratio of 0.08 which is typical of low-metallicty environments (Melnick et al. 1992; Hunt et al. 2004). We used the T_e values from Izotov et al. (2020, 2024). For J150934+373146 and J160810+352809 we used a fixed value of 20,000 K. We have used the $S^{\mathrm{th}}_{1\mathrm{GHz}}$ derived from our Bayesian analysis to estimate the $\mathrm{Flux}^{\mathrm{Exp}}_{\mathrm{H}\beta}$. Specifically we use the values derived from assuming uniform priors which allows us to independently estimate $S^{\mathrm{th}}_{1\mathrm{GHz}}$ using our radio observations alone.

This paper has been typeset from a TEX/LATEX file prepared by the author.